

Rain re-evaporation, boundary-layer/convection interactions, and Pacific rainfall patterns in an AGCM

Julio T. Bacmeister

Goddard Earth Sciences and Technology Center University of Maryland, Baltimore
County, Baltimore, MD 21250

Max J. Suarez

Global Modeling and Assimilation Office, NASA GSFC, Greenbelt, MD 20771

Franklin. R. Robertson

NASA MSFC, Huntsville, AL 35812

Short title:

Abstract. Sensitivity experiments with an atmospheric general circulation model (AGCM) show that parameterized rain re-evaporation has a large impact on simulated precipitation patterns in the tropical Pacific, especially on the configuration of the model’s intertropical convergence zone (ITCZ). Weak re-evaporation leads to the formation of a “double ITCZ” during the northern warm season. The double ITCZ is accompanied by strong correlation between precipitation and high-frequency vertical motion in the planetary boundary layer (PBL). Strong re-evaporation leads to a better overall agreement of simulated precipitation with observations. The model’s double ITCZ bias is reduced. At the same time, correlation between high-frequency (periods < 15 d) vertical motion in the PBL and precipitation is reduced. Experiments with modified physics indicate that evaporative cooling by rain near the PBL top weakens the coupling between precipitation-related heating and vertical motion in high-frequency motions. The strength of high-frequency vertical motions in the PBL was also reduced directly through the introduction of a diffusive cumulus momentum transport (DCMT) parameterization. The DCMT had a visible impact on simulated precipitation in the tropics, but did not reduce the model’s double ITCZ bias in all cases.

Further analyses of mass and water vapor budgets, as well as vertical motion statistics, in the ITCZ complex, show that time-mean, moisture convergence in the southern ITCZ is largely dominated by high-frequency modes, while in the northern ITCZ, time-mean moisture convergence contains large contributions from slower modes. This may explain why the simulated southern ITCZ is more susceptible to parameterization changes that alter high-frequency coupling between moist heating and PBL convergence.

1. Introduction

Accurate simulations of tropical precipitation remain a challenge for atmospheric climate models (AGCMs). Basic dynamical issues such as the relationship between low-level convergence and precipitation remain unresolved. Recent studies suggest that intertropical convergence zones (ITCZs) identified using precipitation or outgoing longwave radiation (OLR) may not always correspond with convergence zones identified using satellite surface wind measurements (e.g.; Liu and Xie, 2002). Earlier Hastenrath and Lamb (1977), using ship-based wind observations, also concluded that surface convergence may exist in the absence of precipitation. Nevertheless, determining the strength of surface wind convergence in nature remains a challenge. Perhaps as a result of this observational gap, little attention has been paid to examining convergence-precipitation coupling in AGCM simulations, even though all the necessary quantities are easily accessible.

A common problem in AGCM precipitation simulations, that may be related to PBL-precipitation coupling, is the so-called double ITCZ bias (e.g.; Meehl and Arblaster, 1998). Many AGCMs form a spurious second ITCZ in the southern hemisphere (8-10°S) under conditions in which observed precipitation is concentrated in a single ITCZ centered around 10 °N. While nature does show hints of a southern ITCZ over the Pacific, particularly during March through May (Zhang, 2001), this feature in AGCMs is usually too strong and persistent, lasting through the northern warm season June-September. The occurrence of double ITCZs in AGCMs leads to large rms errors in simulated precipitation, since it represents a spurious rearrangement of the most intense precipitation on earth. Connections between double ITCZs and other AGCM simulation biases have not been conclusively established. However, it is clearly of concern to climate modelers, if AGCMs are producing large errors in the horizontal distribution of atmospheric latent heating. Finally, the wide distribution and

similar structure of this bias in a variety of AGCMs suggests a the existence of a shared misunderstanding in current implementations of convection parameterizations.

In this study we will examine the connection between PBL convergence and precipitation and the double ITCZ bias in the NSIPP-2 AGCM. A principal motivation for performing this work is a robust sensitivity in the NSIPP AGCM’s tropical precipitation to the strength of rain re-evaporation. With stronger rain re-evaporation the model tends toward a realistic single ITCZ configuration. With weak re-evaporation the model produces a strong double ITCZ. This sensitivity has existed in earlier versions of the NSIPP AGCM despite substantially different formulations of re-evaporation. Although this sensitivity has been useful in empirical “tuning” of the NSIPP AGCM to improve precipitation simulations, the physical origin of the sensitivity has not been explained. Anecdotal evidence from other modeling groups suggests that this sensitivity may exist in some form in other AGCMs (I.M. Held, pers. comm.), and also that other sensitivities may exist to parameters such as cumulus friction (Klein et al. 2004).

The goals of this study are to shed light on mechanisms controlling the formation of double ITCZs in the NSIPP AGCM, and to suggest relevant, parameterization-independent diagnostics that can be applied to other AGCM simulations. The paper is organized as follows. Section 2 provides a description of the AGCM used in this study. Section 3 outlines the AGCM experiments performed. Section 4 presents the basic sensitivity of the model simulations to re-evaporation. Seasonal mean fields are shown, as well as some analysis of vertical profiles, re-evaporation tendencies and high frequency transients. Section 5 describes three experiments with modified physics including changes to the vertical profile of re-evaporation cooling, and the addition of a simple diffusive cumulus momentum transport (DCMT) parameterization. Section 6 analyzes the mass and water vapor budgets in the simulations. This analysis addresses the questions of how re-evaporation supresses precipitation in the southern ITCZ, and

why the suppression operates preferentially on the southern ITCZ.

2. Model Description

We use a development version of the NSIPP-2 AGCM (NSIPP-2.0) for this study. NSIPP-2.0 was developed from the NSIPP-1 AGCM, which was documented in Bacmeister and Suarez (2000) and Bacmeister and Suarez (2002). Simulated seasonal means and responses to inter-annual SST variation in NSIPP-1 were both in good agreement with meteorological analyses (e.g.; Schubert et al., 2001, 2002). The significant modifications to NSIPP-2.0 and NSIPP-1 involve the cloud, boundary layer, and convection schemes. These include introduction of a prognostic cloud scheme in place of the Slingo (1987)-type diagnostic scheme used in NSIPP-1, as well as a simple moist boundary layer entrainment scheme, which is called in addition to the existing first-order dry turbulence parameterization of Louis et al (1982). These modifications were aimed at improving the models simulation of subtropical marine stratus decks, and while they also impact simulated precipitation in the tropics, they do not affect the general nature of the ITCZ sensitivities examined in this study. Cloud fields from NSIPP-2 are examined by Zhang et al. (2004).

The dynamical core of NSIPP-2.0 is the same as in NSIPP-1 and is described in Suarez and Takacs (1996). Radiative effects in NSIPP-2.0 are parameterized using the approach of Chou and Suarez (1992). Land surface effects are parameterized according to Koster and Suarez (1996), and orographic wave drag is treated according to Zhou et al. (1996).

2.1 Convection

Convection in the NSIPP AGCM is parameterized according to the relaxed Arakawa-Schubert (RAS) scheme of Moorthi and Suarez (1992). The implementation of RAS in NSIPP-2.0 is modified to include a convective condensate calculation with

autoconversion to rain. RAS works by invoking a series of linearly-entraining plumes (or “cloud-types”) that detrain at selected levels in the vertical. Consistency is achieved by calculating the entrainment rate necessary to ensure zero buoyancy at the selected level. RAS is flexible as far as the number and distribution of plumes or “cloud-types” tested. Our implementation invokes 30 cloud-types per gridbox per physics time-step. These are drawn at random from a uniform distribution in σ . We also emphasize that our implementation does not include an explicit downdraft parameterization.

2.2 Prognostic cloud condensate scheme

The NSIPP-2 prognostic condensate scheme considers only a single phase of condensate, but tracks two separate species of condensate; a large-scale species $q_{c,LS}$ originating from gridbox condensation and an “anvil” species $q_{c,AN}$ originating from detraining convection. The rationale for this separation is that both the subgrid statistics and the microphysical properties of rapidly processed anvil condensate may be distinct from those of condensate produced by slower, large scale dynamics (e.g. Lawson 2003). The key distinctions in our current scheme are slower autoconversion and higher number densities for $q_{c,AN}$. These higher assumed number densities for $q_{c,AN}$ enter into the optical thickness calculation used by model’s radiation scheme. We impose an arbitrary e-folding time of 3 hours for conversion of $q_{c,AN}$ to $q_{c,LS}$. A third species, convective condensate $q_{c,CN}$ is calculated internally within each RAS cloud-type, but does not interact with the model’s radiation calculation.

2.3 Convective autoconversion and re-evaporation

Our basic approach in parameterizing convective microphysical processes is based on a Lagrangian parcel picture. We estimate an updraft speed for each plume in RAS (Bacmeister 2005) which is combined with the model’s vertical grid spacing to give a time interval for autoconversion in a given model layer. Autoconversion rates are determined from a nonlinear temperature-dependent expression (Sundquist 1988).

The approach used is similar to that in Sud and Walker (1999) although we employ a cruder calculation for the convective updraft speed. Profiles of convective precipitating condensate $q_{p,CN}$ are accumulated over all RAS plumes and then passed to a scheme that accumulates the condensate and also calculates re-evaporation, accretion and surface precipitation fluxes. In addition to precipitating condensate produced by convection, our scheme considers autoconversion of $q_{c,AN}$ and $q_{c,LS}$. These autoconversions are calculated separately using the Sundquist (1988) formulation to give two additional precipitating species $q_{p,AN}$ and $q_{p,LS}$.

Re-evaporation is treated separately for each of the three streams of precipitation (“showers”) $q_{p,CN}$, $q_{p,AN}$, and $q_{p,LS}$. This calculation also proceeds according to a Lagrangian viewpoint. First, an estimate of the local subgrid scale precipitation rate is made using the grid mean precipitation flux and estimates of fractional shower area. A representative particle size for this precipitation is estimated from a Marshall and Palmer (1948) distribution. This particle size gives an evaporation rate, fall speed, ventilation factor and residence time within a given model layer. These quantities are used to calculate a net loss of precipitating condensate due to evaporation during a time step. In NSIPP-2 both liquid and frozen precipitation are treated in the same way. We also allow a fraction of the convective rain shower to be “shielded” from re-evaporation. This is meant to represent rain falling through a saturated environment such as a convective tower or saturated downdraft.

In the experiments discussed here bulk re-evaporation of convective precipitation $q_{p,CN}$ was modified by changing shear-dependent parameters that control the shielded fraction, as well as the relationship between diagnosed updraft areal fraction and convective shower area. Roughly speaking more re-evaporation is allowed in high shear environments in all experiments, but the strength of this shear-dependence is changed to give higher or lower total re-evaporation. Experience with previous versions

of the NSIPP model suggests that the details of the rain re-evaporation scheme are unimportant in producing the sensitivities discussed here. For clarity we will simply refer to three settings of re-evaporation parameters - weak, moderate, and strong. More details on the formulation of the re-evaporation calculation can be found in (Bacmeister, 2005)

3. Description of Experiments

We analyze results from 6 experiments (Table 1). The first three of these, denoted B1, B2, and B3, were performed with the same “baseline” model physics, differing only in the choices made for the rain re-evaporation parameters. These experiments were initialized on June 1 1981 from restarts derived from an existing AMIP simulation and forced with observed SSTs (Reynolds 1996). Exps B1 and B3 ran through December 1987. Experiment B2 was an AMIP style run conducted for the Tropical boundary layer Clouds Climate Process Team and ran through December 1999. For most of the analysis here we will focus on results from 1984 and 1985.

In addition to the three baseline experiments we conducted three experiments with modified physics. In the first of these - H1 - the cooling produced by rain re-evaporation was redistributed in the vertical, i.e., at each time-step, total mass-weighted re-evaporation cooling below 850 hPa was found and then uniformly applied between 850 and 300 hPa. The moistening from re-evaporation was not modified. Thus, moist energy conservation is violated locally, but preserved in a column-integrated sense. The motivation for this experiment was to reduce the direct impact of re-evaporation on boundary layer circulations, while retaining as much of the original moistening profile as possible.

The remaining two experiments M1 and M2 employed a simple diffusive cumulus momentum transport (DCMT) scheme devised for GFDL AM2 model (GFDL Global

Atmospheric Model Development Team, 2004). The scheme simply enhances K_m proportional to the total local cumulus mass flux diagnosed by RAS. The DCMT scheme has been used in the GFDL model with positive effects on both the simulated precipitation and on the simulated spectrum of ENSO variability in coupled mode. Here we apply DCMT in two experiments; M1, with weak re-evaporation settings as in B1, and M2, with moderate re-evaporation as in B2. Exps H1, M1 and M2 were initialized on Dec 1 1983 and run through Dec 31 1985.

All experiments were conducted at a horizontal resolution of 2×2.5 degrees with 40 unequally spaced σ layers. Extensive suites of diagnostic tendency outputs on σ -surfaces were saved as daily averages, along with standard outputs. These additional diagnostics included most of the significant water substance conversion terms such as moistening by re-evaporating rain, which we denote here by \mathcal{R} .

4. Basic Model Sensitivity to Re-evaporation

4.1 Mean seasonal precipitation

Seasonal mean precipitation fields and biases for June-July-August 1984-85 in experiments B1, B2, and B3 are shown in Figures 1 and 2, along with observational estimates of precipitation rates from CMAP (Xie and Arkin, 1997). The results illustrate the important climatological control exerted by the re-evaporation strength in the NSIPP AGCM. Exp B1 with weak re-evaporation (Figs.1a,2a) tends strongly toward a “double ITCZ” configuration, with precipitation rates in excess of 8 mm d^{-1} extending in a narrow, zonally-aligned band along 10S well into the central Pacific. As re-evaporation is strengthened in B2 (Figs. 1b, 2b) and B3 (Figs. 1c, 2c) the double ITCZ in all three tropical ocean basins becomes less pronounced, although the change in the Pacific basin is most noticeable due to its size. In connection with the weakening of the double ITCZ, a dry bias along the equator in the western Pacific in B1 is also

reduced with increased re-evaporation. Overall, the simulations in experiments B2 and B3 appear to be in better agreement with the CMAP climatology. Pattern correlations for the 7-season (1981-87) JJA mean are significantly lower for B1 than for B2 and B3 (Table 1). Wet biases over summertime tropical continents also appear to decrease as rain re-evaporation is strengthened. Over sub-Saharan Africa as well as over the northern Amazon Basin wet biases of over 4 mm d^{-1} exist in Exp B1, while in B3 these regions are nearly bias free.

Unfortunately, not all precipitation biases are reduced by increasing re-evaporation strength in the model. A noticeable deterioration in the simulated precipitation occurs over much of the northern tropical Pacific between Hawaii and southeast Asia (5°N to 20°N and 120°E to 150°W) as re-evaporation increases. Stronger re-evaporation leads to increasing wet biases in this region, culminating in the $>8 \text{ mm d}^{-1}$ biases evident in the “Phillipine Hotspot” (130°E , 15°N) in Exp B3 (Figs. 1c,2c). A JJA dry bias in the Indian Ocean, also becomes more pronounced with increasing re-evaporation. This strong wet bias is associated with excessively strong low-level, monsoon westerlies over Indochina, the Phillipines and surrounding ocean. As will be shown in Section 6, much of the water vapor flowing into this region does so in a strong convergent flow located above the 850 hPa surface. By contrast, in the ITCZs mass and water vapor convergence are largely restricted to the PBL.

We have focused on northern summer because the double ITCZ bias, in models which possess it, is most pronounced during the northern warm season, roughly April-November. During December-February (not shown) some double ITCZ bias remains in our weak re-evaporation simulation. However, overall the DJF precipitation simulations in all 3 experiments are in better agreement with the CMAP climatology.

4.2 Fractional re-evaporation

Figure 3 shows maps of the fraction

$$f = \frac{\sum_{\sigma=1}^0 \mathcal{R}_{\sigma} \frac{\delta p_{\sigma}}{g}}{\mathcal{P}} \quad (1)$$

that is the ratio of the vertical mass integral of the re-evaporation tendency \mathcal{R} to the surface precipitation flux. This quantity provides a measure of re-evaporation “strength” that does not depend on the details of the rain re-evaporation parameterization used. Figure 3 shows that in Exp B1 values of f are below 1 almost everywhere, except over arid continental regions. As expected, in Exps B2 and B3 the re-evaporation fraction increases dramatically. In both experiments values of f are over 1 across most of the tropics and subtropics. Only stratocumulus regions show values of f below 1 in these simulations. In Exp B3 most of the Indian Ocean is characterized by f close to or exceeding 2. That is, over twice as much rain evaporates during its fall through the atmosphere, as makes it to the surface. Much of the southern Pacific ITCZ also possesses $f > 2$.

Table 2 lists domain averages of \mathcal{P}_0 , $\int \mathcal{R}$ and other quantities in the box shaped domains shown in Figure 4. The domain averaged precipitation in the central southern Pacific ITCZ (domain “SITCZ”) for the baseline experiments varies from just over 6.1 mm d⁻¹ in B1 to just under 4 mm d⁻¹ in B3. By comparison the surface evaporation E_0 (column 8) varies little from experiment to experiment, hovering between 5.2 and 5.4 mm d⁻¹ in SITCZ. The difference $E_0 - \mathcal{P}_0$ (last column) is the implied transport water vapor in or out of each domain, with negative numbers implying a net horizontal transport into the domain. Domain SITCZ is a net water vapor sink in Exp B1, but becomes a net source with stronger rain re-evaporation in B2 and B3. For the strongest re-evaporation tried (B3), both ITCZ domains become net sources of water vapor.

Results for two warm season continental domains are also shown: an arid one containing the southwestern US “WUSA”; and a moist one containing the West African

ITCZ region “WAFR”. Despite large differences in the amounts of precipitation and in the fractions of re-evaporated rain, these continental domains exhibit a interesting similarities in their sensitivity to re-evaporation. Both rain and surface evaporation decrease markedly with increasing rain re-evaporation. This is in contrast to the situation over ocean (SITCZ and NITCZ) where surface evaporation is largely unaffected by rain re-evaporation. Note the large values of f (column 6, Table 2) in WUSA for all experiments. These may be related to the lack of an explicit downdraft parameterization in the model.

Observational estimates of domain averaged precipitation from CMAP are also shown in Table 2. Comparisons of these with the simulation results tend to confirm that Exp B2 possesses the “best” precipitation, as implied by the pattern correlations and normalized variances in Table 1. Comparison of observations and simulations in WUSA show that our model has a pronounced dry bias in this region, probably related to excessive re-evaporation of rain. Unfortunately, global observational estimates of $\int \mathcal{R}$ are not currently available.

4.3 Vertical profile of Rain Re-evaporation

Figure 5 shows seasonal mean profiles of re-evaporation tendency \mathcal{R} , horizontally-averaged within Box NITCZ. This boxes straddles the northern ITCZ during JJA. Re-evaporation in Exps B2 and B3 is generally strong (1 to 2 g kg⁻¹ d⁻¹) throughout the lowest 500 hPa of the atmosphere. A minimum in \mathcal{R} occurs in the upper portion of the model PBL where relative humidities are high, but both within the PBL and immediately above the PBL-top re-evaporation is high. It is worth noting that the re-evaporation profile in Exp B1 is dominated by evaporation of large-scale and anvil precipitation ($q_{p,AN}$ and $q_{p,LS}$) which are unaffected by the shear-dependent, re-evaporation parameters varied in this study.

Re-evaporation of condensate is not a process for which we have direct observational data to validate models. However, efforts are underway to infer some of the gross features of re-evaporation from TRMM radar precipitation rate profiles. Initial examination suggests that significant disagreements may exist between simulated re-evaporation profiles and TRMM inferences (pers comm. F. R. Robertson).

4.4 Water vapor distribution

Figure 6 shows mean water vapor profiles for Exps B1-B3 in boxes SITCZ and NITCZ along with estimates from NCEP (Kalnay et al., 1995) and ERA40 (Simmons and Gibson, 2000) re-analyses. In NITCZ (Fig. 6, top) the two re-analyses disagree by nearly 3 g kg^{-1} over much of the layer between below 300 hPa. The three model experiments generally lie in between the two re-analysis profiles. The profile for Exp B3 is up to 2 g kg^{-1} wetter than that for B1 with the largest differences centered around 700 hPa. The profile for B2 lies between those for B1 and B3. In Box SITCZ (Fig. 6, bottom) the situation is somewhat different. The q -profiles from our 3 model experiments are quite similar to the corresponding profiles in NITCZ, with B3 the wettest, B1 the driest, and B2 in the middle. The NCEP re-analysis profile in SITCZ is also similar to that in NITCZ. However, the ERA40 re-analysis profile is significantly drier, and here agrees closely with the NCEP profile. Generally speaking it is clear that increasing re-evaporation in our model leads to mid-tropospheric moistening. However, the differences in q -profiles for different re-evaporation strength appear to be comparable to uncertainties in re-analysis q -profiles. Comparison with SSMI total precipitable water (TPW) measurements (not shown) exhibit a small but worsening global mean wet bias as re-evaporation increases from B1 to B3, although the spatial distribution of simulated TPW improves.

4.5 Relation of low-level convergence and Rainfall

The strength of the high-frequency coupling between low-level flow convergence and precipitation in nature is still not well known (e.g. Gu and Zhang, 2002). However, there are indications that the connection between low-level convergence and precipitation at time-scales of several days and shorter may not be as strong as commonly assumed. We examine this coupling in our simulations by looking at the correlation of daily mean vertical motion at 850 hPa ω_{850} with daily rainfall \mathcal{P} in our simulations. Straightforward time-series correlations are calculated at each model gridpoint using results from the 183-day period May 1-October 31, 1985. A 15-day, high pass Lanczos filter (Duchon 1979) was first applied to each field to remove low-frequency variability. Figure 7 shows maps of the correlation $r(\tilde{\omega}_{850}, \tilde{\mathcal{P}})$, where $\tilde{\omega}_{850}$ and $\tilde{\mathcal{P}}$ denote the time-filtered fields. There is a pronounced difference in the strength of this correlation as re-evaporation changes. For weak re-evaporation as in B1 (Fig. 7a) the correlations are over 0.8 over much of the tropical Pacific. By contrast, with strong re-evaporation as in B3 (Fig. 7c), correlations are generally between 0.4 and 0.6, and fall below 0.4 over large portions of the warm pool and the southern ITCZ region (0-10°S, 180-150°W). A strong reduction in $r(\tilde{\omega}_{850}, \tilde{\mathcal{P}})$ is notable along the equator in the western Pacific as re-evaporation increases.

The rms amplitude of $\tilde{\omega}_{850}$ is shown in Figure 8. Maps of $\sqrt{\tilde{\omega}_{850}^2}$ show that the pattern of dynamical variability is not straightforwardly related to the correlation patterns in Fig. 7. For example, $\sqrt{\tilde{\omega}_{850}^2}$ over the northern warm pool and western tropical Pacific (0-20°N, 120°E-180°E) is similar in B1, B2 and B3 with values around 50-70 hPa d⁻¹. However, $r(\tilde{\omega}_{850}, \tilde{\mathcal{P}})$ in the same region varies from 0.6 to >0.8 in B1 to <0.4 in B3. Interestingly, this is the region in which larger re-evaporation appears to lead to a strengthening wet bias. It appears safe to conclude that this bias, and precipitation generally, in this region is not controlled principally by boundary layer/precipitation interactions. By contrast, over both ITCZ regions the dynamical

variability weakens systematically as re-evaporation increases. West of 150°W B1 shows values of $\sqrt{\tilde{\omega}_{850}^2}$ of 60 to 80 hPa d⁻¹, while B3 shows values of 30 to 50 hPa d⁻¹. The decrease in dynamical variability over the southern ITCZ between Exps B1 and B3 is especially dramatic.

Figure 9 shows Hovmueller diagrams of \mathcal{P}_0 and $\tilde{\omega}_{850}$ along 8S for Exps B1 and B3. The association of high precipitation rates with westward moving high frequency disturbances in both experiments is clear. There is a general connection between areas of high precipitation (dark blue) in the left panels with areas of strong upward motion at 850 (blue-purple) in the right panels. As expected, the variability is stronger in Exp B1 (top panels), although the difference for variability in ω_{850} is not as pronounced as for precipitation.

The simulated ITCZ disturbances in Fig. 9 appear to amplify as they move west. Figure 10a shows probability density functions (PDFs) of ω_{850} (unfiltered) in a box immediately west of the South American coast (10S to 6S, and 110W to 97.5W) for May-October 1985. This box is situated over cool water and can be thought of as the "entrance" region for disturbances propagating westward along the southern ITCZ. This figure shows that the amplitude distribution of ω_{850} , before strong interactions with moist heating have occurred, is remarkably similar in Exps B1 (black curve) and B3 (red curve). However, further west (10S to 6S, and 162.5E to 175E) the PDFs diverge markedly (Fig. 10b). In B1 the PDF of ω_{850} becomes highly skewed, with an extensive tail region at large negative values of ω_{850} , i.e., upward motion, and a concentrated peak at small positive values. This means that even at the model grid scale there is a distinctly "convective" character to vertical motion, with rare but intense updrafts embedded in extensive but weak subsidence. For B3 the PDF in the western box is also somewhat more skewed than in the entrance region, but the overall shape of the PDF is much less distorted.

Taken together the results in this section imply the existence of a similar background dynamical variability in Exps B1 and B3. This “seed” variability is then amplified to different degrees by interactions with precipitation, with stronger feedback occurring when rain re-evaporation is weak. The possible nature of this interaction will be examined by direct experimentation with altered model physics (Section 5) and by analysis of water vapor budgets in the ITCZ (Section 6)

We have not attempted a detailed comparison of our simulated x-t spectra of rainfall or vertical motion with observations (e.g.; Wheeler and Kiladis, 1997; Gu and Zhang, 2001). However, a cursory look at our model’s background spectra of precipitation along the ITCZ suggest at least a qualitative resemblance with the background OLR spectra in Gu and Zhang (2001).

5. Experiments with Altered Physics

5.1 *Vertically-redistributed Re-evaporation cooling*

From the results shown in Section 4 we speculate that the formation of ITCZs in our simulations is at least partly driven by strong coupling between boundary layer convergence and precipitation-related, moist heating. The disappearance of double ITCZs with increased re-evaporation suggests that this coupling is interrupted by evaporative cooling in or near the PBL. To test this hypothesis, we performed an experiment, H1 (Table 1), in which we arbitrarily removed cooling driven by rain re-evaporation below 850 hPa. This experiment used “strong” re-evaporation settings as in B3. To conserve at least column-integrated moist static energy, we calculated a mass-weighted integral of the re-evaporation cooling between 850 hPa and the surface. This mass-weighted cooling was then redistributed uniformly between 300 and 850 hPa. The corresponding moistening profile was not altered. The motivation for this procedure was to remove the low-level cooling from the strong re-evaporation case while

minimizing modifications to the moistening profile.

Figure 11a shows seasonal mean JJA 1984-85 precipitation from H1. A strong double ITCZ re-appears in this experiment even though re-evaporation parameters are as in Exp B3 (Fig. 1c, 2c). In fact, Figure 11b shows that the fraction of re-evaporated rain is generally higher than in B3. Domain averages of precipitation and re-evaporation related quantities for H1 are shown in Table 2. Figure 11c shows $r(\tilde{\omega}_{850}, \tilde{\mathcal{P}})$ for H1. Comparison with the same quantity for Exps B1, B2, and B3 (Fig. 7) reveals that that $r(\tilde{\omega}_{850}, \tilde{\mathcal{P}})$ is even higher in H1 than it was in B1. Thus, this experiment suggests that the low-level cooling associated with rain re-evaporation does in fact disrupt positive feedback between low-level convergence and precipitation. Artificially removing the low-level cooling from an experiment with strong re-evaporation restores the feedback and leads to the re-appearance of strong double ITCZ bias in the model.

5.2 Diffusive Cumulus Momentum Transport (DCMT)

As described in the introduction, simulations of tropical precipitation in other AGCMs exhibit sensitivities to other processes. The GFDL AGCM has shown a strong sensitivity to the presence of a diffusive cumulus momentum transport (DCMT) parameterization (Klein et al., 2004). The GFDL DCMT scheme is formulated as a momentum diffusivity proportional to the total cumulus mass flux passing through a given level. Its effects are largest at low-levels where all clouds, both weakly entraining deep clouds, as well as strongly entraining shallow clouds are present. When DCMT is present in GFDL model, the simulated tropical precipitation is improved, in particular the model’s tendency to form double ITCZs is reduced.

We performed two experiments with DCMT (Table 1). One, M1, used re-evaporation parameters as in B1. In the baseline model these parameters led to a pronounced double ITCZ bias (Figs. 1a, 2a). The second experiment with DCMT,

M2, used re-evaporation parameters as in B2. In the baseline model these parameters produced a reasonable simulation of precipitation overall, with a weak double ITCZ bias (Figs 1b,2b). The 1984-85 JJA mean precipitation for Exps M1 and M2, is shown in Figures 12a and 12c. The small double ITCZ bias in Exp B2 is further reduced by the added DCMT in M2, although the wet bias in the northwestern tropical Pacific (Eq-20°N, 120°E-180) appears to have been exacerbated, much as in Exp B3. On the other hand the strong double ITCZ bias in the Pacific in B1 is not qualitatively reduced by the added DCMT in M1. There are a number of subtle differences between precipitation fields in M1 and B1. The northern ITCZ in M1 is somewhat weaker and more diffuse looking than in B1, particularly in the eastern Pacific between 150°W and 120°W. Nevertheless, a strong, well developed spurious ITCZ persists in the Pacific around 10°S from 150°E to around 130°W. Interestingly, in the Atlantic, there is a more distinct reduction in the double ITCZ bias in Exp M1.

The correlation $r(\tilde{\omega}_{850}, \tilde{\mathcal{P}})$ (Figures 12b and 12d) shows slight increases with added DCMT primarily along the eastern margins of the Pacific ITCZs, and also in the dry band along the Equator. In regions of strong precipitation $r(\tilde{\omega}_{850}, \tilde{\mathcal{P}})$ appears relatively insensitive to DCMT. Thus, changes in precipitation patterns between B1 and M1 or B2 and M2 are not brought about by changes in the coupling strength of the PBL-precipitation coupling.

Figures 10c and 10d show PDFs of ω_{850} in M1 and M2. In the eastern Pacific (Fig. 10c) the PDFs for M1 and M2 are similar to each other and to those of B1 and B3 (Fig. 10a). This suggests that the addition of DCMT to the model does not reduce the “background” level of dynamical variability in the model. However, in the core of the southern ITCZ region (Fig. 10d) it is clear that the addition of DCMT reduces the magnitude of ω fluctuations compared with the baseline experiments (Fig. 10b). This is evident in the reduced spread of the PDF for M1 (solid light blue) compared with that

for B1. The PDF for M1 shows clear evidence of negative skew, which suggests that the dissipative effects of DCMT do not eliminate feedbacks between moist heating and PBL convergence. However, the negative tail in M1 is less pronounced, with more frequent weaker updrafts, while the peak associated with ubiquitous weak subsidence is also less pronounced than in B1.

6. Convective and Large-Scale Transports in the ITCZs

Our results suggest the existence of a feedback between high-frequency, low-level convergence and precipitation, which contributes to the maintenance of the spurious ITCZ. The feedback is weakened by low-level cooling from rain re-evaporation, and as a consequence our model’s double ITCZ bias is reduced when parameterized re-evaporation is made stronger. The effects of DCMT are more ambiguous, yet it is clear that directly changing the character of dynamical variability in the ITCZs also has an important impact on the resulting simulation of tropical precipitation. In this section, we examine convective transports, as well as mass and water budgets in the ITCZ complex, to understand the relationship between convection, low-level convergence and precipitation. This analysis also suggests how the southern ITCZ and the northern ITCZ differ in their response to high-frequency low-level convergence.

6.1 *Convective fluxes*

Figure 13 shows longitude profiles of total, cloud-base, convective mass flux ϕ_{CB} from RAS along 8°S and 8°N averaged over May-October 1985. The striking aspect of this figure is the similarity in the magnitude of the convective mass fluxes, everywhere except in the Pacific warm pool region (100°E to 140°E along 8°N), where fluxes in B3 are substantially higher. Along the southern ITCZ (Fig. 13b), the total cloud-base convective mass flux in both experiments shows little sensitivity to re-evaporation. In fact, somewhat higher mass fluxes exist in Exp B3 (dashed curve), which does not have

a pronounced double ITCZ in precipitation. Thus, it is clear that re-evaporation in our model does not suppress precipitation in the southern ITCZ by suppressing convection overall. Vertical profiles of convective mass flux (not shown) show some differences between experiments, but these are relatively small compared to the overall fluxes.

The water vapor flux entering convective updrafts is given by $\phi_{CB}q_{CB}$ where q_{CB} is the specific humidity in the sub-cloud layer (here an average of the lowest two model layers). We calculate this flux from daily values of ϕ_{CB} and q_{CB} so that any transient correlations between convection and PBL humidity are included. The mean of this quantity over May-October 1985 is plotted in Figs 13c and 13d, along with the corresponding average of total precipitation. Here again, the differences between $\phi_{CB}q_{CB}$ are opposite to those in precipitation for the southern ITCZ. Consistent with its generally higher mean values of ϕ_{CB} , Exp B3 has higher $\phi_{CB}q_{CB}$ than Exp B1. The ratio of precipitation to $\phi_{CB}q_{CB}$ is another measure of precipitation efficiency like f in (1). This quantity is shown in Fig 13e,f. As expected this efficiency is lower overall in Exp B3 with high re-evaporation, although interestingly, over parts of the northern ITCZ efficiencies in B3 are higher. Nevertheless, over the southern ITCZ, efficiency in Exp B3 is systematically less than that in B1. The largest proportional decreases in precipitation efficiency caused by increased re-evaporation occur around 120 °W in the northern ITCZ and between 180 and 150 °W in the southern ITCZ.

The mean, May-October 1985, surface evaporation \mathcal{E} along 8°S and 8°N for B1 and B3 is plotted in Figs 13c and 13d as well. As suggested by the budgets in Table 2, evaporation is a relatively featureless quantity, both in physical space and parameter space. With the exception of a notable enhancement in evaporation over the western warm pool region in Exp B3 (Fig. 13c, 90°E-130°E), ITCZ evaporation values hover between 5 and 7.5 mm d⁻¹. It should be noted that even in the warm pool region of B3, the increased evaporation is only about 1/3 as large as the increase in precipitation

going from B1 to B3, and less than 1/10 as large as the increases in $\phi_{CB}q_{CB}$. The lack of structure in the evaporation suggests that, at least locally, evaporation feedbacks do not play a major role in maintaining the ITCZ in our model.

6.2 Horizontal Transport of Water Vapor

Figure 13 shows that the southern ITCZ region in our model contains strong convective, cloud-base fluxes of water vapor that cannot be supplied by local surface evaporation. Figure 14 shows a number of vertically-integrated, mass-weighted, horizontal water vapor transport terms from Exps B1, B3 and H1. The first row (Figs. 14a,f,k) shows maps of the time-mean of

$$\mathcal{T}_1^0 \equiv - \sum_{\sigma=1}^0 \nabla_h \cdot q_\sigma \mathbf{v}_\sigma \frac{\delta p_\sigma}{g} \quad (2)$$

the column integral of the total, mass-weighted, horizontal water vapor flux convergence for the period JJA 1995. Daily mean values of all quantities were used for the sum in (2). The quantity \mathcal{T}_1^0 should equal the local value of $\mathcal{P} - \mathcal{E} + \partial_t(TPW)$, where TPW is the total precipitable water in the column. We examined daily time series of \mathcal{T}_1^0 at individual grid points and found that water vapor budgets closed within truncation errors due to different finite difference formulations in (2) and in the model.

Since the model evaporation field lacks structure compared with precipitation (e.g., Figs. 13c,d), and time-mean values of $\partial_t(TPW)$ are small, the patterns of \mathcal{T}_1^0 in Figs. 14a,f,k closely reflect the precipitation patterns in each experiment, with positive values of \mathcal{T}_1^0 corresponding approximately to \mathcal{P} larger than 5 to 7.5 mm d⁻¹. The second and third rows of Fig. 14 separate the total water vapor flux convergence roughly into a low-level, or PBL, component $\mathcal{T}_1^{0.85}$, where the subscript and superscript indicate new limits for the summation performed in (2), and a free-tropospheric component $\mathcal{T}_{0.85}^{0.2}$. In both ITCZs $\mathcal{T}_1^{0.85}$ (Figs. 14b,g,l) tends to exceed the total water vapor convergence \mathcal{T}_1^0 . Even in B3 (Fig. 14g), positive $\mathcal{T}_1^{0.85}$ in the southern ITCZ extends well east of

150°W. Overall, the pattern and magnitude of $\mathcal{T}_1^{0.85}$ appear to show more similarity across experiments than is the case for \mathcal{T}_1^0 , although $\mathcal{T}_1^{0.85}$ is clearly reduced in B3 over the southern ITCZ. In the northern ITCZ, $\mathcal{T}_1^{0.85}$ is quite similar in all 3 experiments shown, with peak values in the eastern Pacific (100°W) of over 16 mm d⁻¹.

The free tropospheric water vapor flux convergence $\mathcal{T}_{0.85}^{0.2}$ (Figs. 14c,h,m) shows that the eastern portions of all simulated ITCZs export water vapor above the PBL. This loss of water vapor is most pronounced in Exp B3 (Fig. 14h) and weakest in H1 (Fig. 14m). However, in all experiments, negative $\mathcal{T}_{0.85}^{0.2}$ is strong enough to overcome low level moisture convergence in the eastern extreme of the southern ITCZ, thereby limiting the eastward extension of southern “ITCZ” in precipitation. In B3, net convergence of water vapor $\mathcal{T}_1^0 > 0$ is confined west of the Dateline. The eastern extremes of the simulated northern ITCZs also exhibit large free-tropospheric divergence of water vapor, with values well past -8 mm d⁻¹ in B3 for example. However, low-level convergence here is so strong that these regions retain strong net water vapor convergence, and therefore remain zones of intense precipitation as well. Note also the large area of strong, free-tropospheric water vapor convergence over the Pacific warm pool region in B3. This suggests that a significant part of the large wet bias seen in Fig. 1 over the same region is fueled by mid-tropospheric transport of water vapor.

The remaining panels in Fig. 14 show a breakdown of $\mathcal{T}_{0.85}^{0.2}$ into a convergent flow component (Figs. 14d,i,n),

$$\mathcal{C}_{0.85}^{0.2} \equiv - \sum_{\sigma=0.85}^{0.2} q_{\sigma} \nabla_h \cdot \mathbf{v}_{\sigma} \frac{\delta p_{\sigma}}{g} \quad (3)$$

and an advective component (Figs. 14e,j,o).

$$\mathcal{A}_{0.85}^{0.2} \equiv - \sum_{\sigma=0.85}^{0.2} \mathbf{v}_{\sigma} \frac{\delta p_{\sigma}}{g} \cdot \nabla_h q_{\sigma} \quad (4)$$

where $\mathcal{T}_{0.85}^{0.2} = \mathcal{C}_{0.85}^{0.2} + \mathcal{A}_{0.85}^{0.2}$. The convergent-flow component $\mathcal{C}_{0.85}^{0.2}$ dominates in all cases within the ITCZs, although $\mathcal{A}_{0.85}^{0.2}$ approaches values of about a third of those attained

by $\mathcal{C}_{0.85}^{0.2}$. In B3 the advective loss of water vapor above the central and eastern ITCZs appears especially well organized. Nevertheless, it appears that over the ITCZs the dominant mechanism responsible for removal of water vapor in the overlying free troposphere is transport by locally-divergent flow.

The major effects of re-evaporation and its associated cooling appear to be; (1) to reduce the strength of the time-mean PBL water vapor flux convergence in the southern ITCZ; and (2) to increase water vapor removal by transport in the free troposphere above both ITCZs. Both effects contribute to eliminating the double ITCZ in Exp B3, while the lack of an appreciable re-evaporation impact on $\mathcal{T}_1^{0.85}$ in the northern ITCZ may explain in part why it is resilient to increased re-evaporation.

6.3 Time behavior of boundary layer convergence

Analysis of the $\mathcal{T}_1^{0.85}$ calculations in all experiments shows that it is dominated by the convergent flow component $\mathcal{C}_1^{0.85}$, and that furthermore both time and height variations of q within the PBL are of secondary importance in $\mathcal{C}_1^{0.85}$. So, we can write

$$\mathcal{T}_1^{0.85} \approx - \overline{q_{PBL}}^{tz} \sum_{\sigma=1}^{0.85} \nabla_h \cdot \mathbf{v}_\sigma \frac{\delta p_\sigma}{g} \quad (5)$$

and, over oceans the vertical sum of the mass divergence in (5) can be approximated by ω_{850} , so that we have finally

$$\mathcal{T}_1^{0.85} \approx - \overline{q_{PBL}}^{tz} \omega_{850}. \quad (6)$$

Thus, we can understand the basic features of water vapor transport below 850 hPa in our model by examining ω_{850} . Our earlier analysis of ω_{850} (c.f. Figs. 8-10) showed that transients in ω_{850} within the ITCZs were generally weaker with stronger re-evaporation. This is reflected in the JJA-mean longitude profiles of $\sqrt{\tilde{\omega}_{850}^2}^t$ shown in Figs. 15a-d. Reductions in transient activity are especially noticeable in the southern ITCZ between 150°E and 120°W, where Exps B1 (Fig. 15a) and M1 (Fig. 15c) show $\sqrt{\tilde{\omega}_{850}^2}^t$ well over 50 hPa d⁻¹, while the corresponding experiments with stronger re-evaporation have $\sqrt{\tilde{\omega}_{850}^2}^t$

around 30 hPa d⁻¹.

Of greater interest is the relationship between $\tilde{\omega}_{850}$ and the straightforward time means of ω_{850} , shown by the thick dashed and solid curves in Figs. 15a-d. In the southern ITCZ (dashed curves) all experiments show a remarkable correlation between $-\overline{\omega_{850}}^t$ and $\sqrt{\tilde{\omega}_{850}^2}^t$. Mean upward motion along the southern ITCZ only occurs where strong high-frequency variability in ω_{850} is also found, e.g., 150°E-180. In the northern ITCZs there is also a degree of correlation between $\sqrt{\tilde{\omega}_{850}^2}^t$ and $-\overline{\omega_{850}}^t$ especially on the western side of the Pacific. However, in the eastern portion of the northern Pacific ITCZ, $\sqrt{\tilde{\omega}_{850}^2}^t$ is relatively constant at around 50 hPa d⁻¹ while the magnitude of $-\overline{\omega_{850}}^t$ decreases strongly towards the west, from around 90 hPa d⁻¹ near 90°W to 20 hPa d⁻¹ near the dateline.

The nearly linear relationship between $\sqrt{\tilde{\omega}_{850}^2}^t$ and $-\overline{\omega_{850}}^t$ in the southern ITCZ suggests that the time mean vertical motion there is determined by high-frequency transient events with intense upward motion. This is consistent with the highly-skewed, asymmetric structure of the ω_{850} -PDFs in Figs. 10a-10d. These PDFs consist of a core peak centered somewhat above zero, representing weak ubiquitous subsidence, with an extended, decaying tail representing updrafts which become increasingly rare as they become more intense. On the other hand the PDFs for B1 and B3 in the eastern portion of the northern ITCZ (Fig. 10e) are more suggestive of a bimodal distribution, with a secondary broad peak at -100 to -300 hPa d⁻¹, representing what may be active periods of convection, superimposed on skewed PDFs like those found in the southern ITCZ. We have not analyzed the time-behavior of our model ω_{850} field in detail, but the relative lack of correlation between $\sqrt{\tilde{\omega}_{850}^2}^t$ (15-day filtered ω) and $-\overline{\omega_{850}}^t$ in the northern ITCZ, suggests that these modes have timescales longer than 15 days. Such periods occurring on timescales of several weeks, and possibly related to the MJO, have been identified in observations over the eastern Pacific ITCZ by Maloney and Hartmann (2001) and

Raymond et al. (2004).

7. Summary and Discussion

We examined the effect of parameterized rain re-evaporation on tropical precipitation \mathcal{P}_0 in a series of AGCM experiments. We found that stronger rain re-evaporation led to reductions in the double ITCZ bias in our model's simulated precipitation. The effect of rain re-evaporation on seasonal mean precipitation appears to be at least partially due to low-level evaporative cooling, which prevents feedbacks between convective heating and PBL convergence in high frequency ($T < 15$ d) modes. This is evident in weakened correlations between filtered time series of vertical motion at 850 hPa ω_{850} and precipitation in Pacific ITCZ region as re-evaporation increases (Fig. 7). An experiment in which strong re-evaporation was used, but where evaporative cooling was eliminated below 850 hPa, yielded an intense double ITCZ, and high ω_{850} - \mathcal{P}_0 correlations, despite large column integrated re-evaporation moistening (Fig. 11). Probability density functions (PDFs) of ω_{850} showed an interesting shift from sharply peaked symmetric distributions in the far eastern section of the southern ITCZ to highly skewed, asymmetric distributions in the core region of the southern ITCZ (Fig. 10). The tails of these PDFs represent rare but intense updrafts associated with bursts of convection. The degree of asymmetry in the PDFs increases with decreasing re-evaporation, i.e., for stronger double ITCZ bias. We interpret the asymmetry in the PDFs of ω_{850} as another manifestation of the feedback between low-level convergence and precipitation which occurs in high-frequency westward propagating disturbances traveling along the ITCZ.

An obvious question is why eliminating or weakening the feedbacks between low-level convergence and precipitation has an apparently much weaker effect on the northern ITCZ. We addressed this question by examining convective transports and

mass and water vapor budgets in the ITCZs. Surface evaporation was found to a relatively “featureless” field in the ITCZ complex, with little variation geographically or between experiments. Therefore, the strong variations in precipitation we found in our experiments must be balanced by water vapor transport. As expected, water vapor convergence below 850 hPa is the dominant term over most of the ITCZ system (Fig. 14), so precipitation largely follows this field. Nevertheless, we note that significant water vapor divergence between 850 and 200 hPa is found over the eastern portions of all ITCZs (Fig. 14c,h,m). This divergence is strongest in Exp B3, and contributes to significant reductions in the extent and magnitude of the total vertically integrated water vapor convergence in both ITCZs. The effect is more noticeable in the southern ITCZ due to relative weakness of low level water vapor convergence there.

To understand why low level convergence is generally weaker in the southern ITCZ we compared the variance of high-frequency $\tilde{\omega}_{850}$ fluctuations with the time mean profiles of ω_{850} in both ITCZs (Fig. 15). In the southern ITCZ of all experiments there is a remarkable, nearly linear relationship between $\overline{\omega_{850}}^t$ and $\sqrt{\overline{\tilde{\omega}_{850}^2}}^t$. This suggests that in the southern ITCZ the time mean convergence is largely determined by the integrated effect of high-frequency convergence bursts. This is consistent with the skewed, highly asymmetric PDFs in Figs. 10b and 10d, in which both the variance and the mean are determined by the updraft tail region (as they would be, for example, in an exponential PDF). On the other hand in the northern ITCZ $\overline{\omega_{850}}^t$ and $\sqrt{\overline{\tilde{\omega}_{850}^2}}^t$ appear to be less tightly related. This implies the existence of a significant component of ω_{850} variability with time scales longer than 15 days. PDFs of ω_{850} from the northern ITCZ (Fig. 10e) exhibit hints of a bimodal structure, with a broad, secondary mode peaking at relatively strong values of upward motion $\approx -200 \text{ hPa d}^{-1}$. We suggest that re-evaporative cooling has less effect on low frequency, perhaps remotely forced modes in ω_{850} . This may explain why re-evaporation is less effective in reducing the strength of the northern

ITCZ, where a significant portion of the total water vapor convergence appears to be driven by such modes.

Experiments with a simple diffusive Cumulus momentum transport scheme (DCMT) were encouraging in that they suggested the Pacific ITCZs will respond directly to a reduction in dynamical variability in the tropics. However, the effects of DCMT in our model were ambiguous. While variability in ω_{850} along the ITCZs was somewhat reduced, the time-mean ω_{850} in the two experiments with DCMT remained comparable to its values in the corresponding experiments without DCMT. The depth of the convergence layer also appeared to increase substantially with DCMT (Fig. 15e). The addition of DCMT did little to eliminate the double ITCZ in the case of weak re-evaporation (Fig. 12a), although with moderate re-evaporation (Fig. 12c) added DCMT largely eliminated the weak bias present in the corresponding experiment without DCMT (Fig. 1b). We conclude that our implementation of DCMT is not vigorous enough to compete with the strong convergence-precipitation feedbacks present in the model with weak re-evaporation. However, in the case of stronger re-evaporation, with reduced convergence-precipitation feedbacks, additional DCMT can effectively counteract the growth of disturbances moving along the southern ITCZ.

Recently, Wu et al. (2003) have shown improvement in CCM3's simulated seasonal evolution of the ITCZ, when a CMT scheme (Zhang and Cho, 1993) was introduced. The relationship of those results to the present study are not yet clear. However, it is of interest that some form of CMT is found to alleviate tropical precipitation biases to some degree, in at least three different AGCMs.

Gu and Zhang (2001) categorize theories of ITCZ formation in to two broad categories 1) SST forced, and 2) internally forced by atmospheric dynamics. Category (2) is further divided into zonally-symmetric and zonally-asymmetric theories. In our model, the connection of high-frequency PBL convergence and precipitation in

the southern ITCZ is suggestive of the wave-driven dynamical mechanisms proposed by Holton et al. (1971), Chang (1973) and Lindzen (1974), and later examined in Aquaplanet GCM simulations by Hess et al. (1991). The situation in our simulated northern ITCZ is not so clear. Here, PBL convergence appears to have an important mode of variability at time scales longer than 15 days. This may be related to SST forced circulations or to slower (seasonal-intraseasonal) internal atmospheric modes (e.g. Maloney and Hartmann, 2001, Raymond et al., 2004).

We hope these results will encourage modelers to examine a number of relatively-simple, parameterization-independent diagnostics of precipitation processes in their models. Example of such diagnostics examined here include; the ratio of re-evaporated rain to rain reaching the surface, profiles of domain-averaged re-evaporation moistening, correlations of high-frequency time series of vertical motion and precipitation, and PDFs of PBL convergence. This list is certainly insufficient, but we believe more detailed examination of atmospheric water budgets and high-frequency precipitation and dynamical variability in climate models is called for despite the relatively poor observational basis available for validation. These analyses may reveal new dynamically-significant similarities between models that suffer similar precipitation biases.

References

- Bacmeister, J. T., P. J. Pegion, S. D. Schubert, and M. J. Suarez, 2000: Atlas of seasonal means simulated by the NSIPP-1 atmospheric GCM, *NASA Technical Memorandum 104606*, **17**, 194pp.
- Bacmeister, J. T. and M. J. Suarez, 2002: Wind Stress simulations and the equatorial momentum budget in an AGCM. *J. Atmos. Sci.*, **59**, 3051–3073.
- Bacmeister, J. T., 2005: Moist processes in the GEOS5 AGCM. (available at <http://gmao.gsfc.nasa.gov/systems/geos5/MoistProcessesGEOSv2.pdf>).
- Chou, M.-D. and M. J. Suarez, 1994: An efficient thermal infrared radiation parameterization for use in general circulation models. NASA Technical Memorandum, 104606, **10**, 84pp.
- Duchon, C. E., 1979: Lanczos filter in one and two dimensions. *J. Applied Meteor.*, **18**, 1016-1022.
- Gu, G., and C. Zhang 2001: A spectrum analysis of synoptic-scale disturbances in the ITCZ. *J. Climate*, **14**, 2725-2739.
- Gu, G., and C. Zhang 2002: Westward-propagating synoptic-scale disturbances and the ITCZ. *J. Atmos. Sci.*, **59**, 1062-1075.
- Hess, P. G., D. S. Battisti, and P. J. Rasch, 1993: Maintenance of the intertropical convergence zones and the large scale tropical circulation on a water-covered earth. *J. Atmos. Sci.*, **50**, 691-713.
- Holton, J. R., J.M. Wallace, and J. A. Young, 1971: On boundary layer dynamics and the ITCZ, *J. Atmos. Sci.*, **28** 275-280.
- Kalnay, E., M. Kanamitsu, R. Kistler, W. Collins, D. Deaven, J. Derber, L. Gandin, S. Sara, G. White, J. Woollen, Y. Zhu, M. Chelliah, W. Ebisuzaki, W. Higgins, J.

- Janowiak, K. C. Mo, C. Ropelewski, J. Wang, A. Leetma, R. Renolds, R. Jenne, 1995: The NMC/NCAR reanalysis project. *Bull. Am. Met. Soc.*, **77**, 437-471.
- Klein, S. A., and GFDL Atmospheric Model Development Team, 2004: The new GFDL global atmospheric and land model AM2/LM2: Evaluation with prescribed SST simulations, (*J. Climate*, **to appear**).
- Koster, R. D., and M. J. Suarez, 1996: Energy and water balance calculations in the Mosaic LSM. *NASA Technical Memorandum 104606*, **9**, 69pp.
- Lawson, P., 2003: A comparison of microphysical properties of wave, cirrus and anvil clouds., CRYSTAL-FACE Science Team Meeting, Feb. 2003, (http://cloud1.arc.nasa.gov/crystalface/presentations_files/250p_Lawson.pdf)
- Lee, M.-I., I.-S. Kang, and B. E. Mapes, 2003: Impacts of cumulus convection parameterization on aqua-planet AGCM simulations of tropical intraseasonal variability. *J. Meteor. Soc. Japan*, **81**, 963-992.
- Lindzen, R. S., 1974: Wave-CISK in the tropics, *J. Atmos. Sci.*, **31**, 156-179.
- Louis, J., M. Tiedtke, J. Geleyn, 1982: A short history of the PBL parameterization at ECMWF, in *Proceedings, ECMWF Workshop on Planetary Boundary Layer Parameterization, Reading, U. K.*, p59-80.
- Maloney, E. D., and D. L. Hartmann, 2001: The Madden-Julian oscillation, barotropic dynamics, and north Pacific tropical cyclone formation. Part I: Observations. *J. Atmos. Sci.*, **58**, 2545-2558.
- Marshall, J. S., and W. M. Palmer, 1948: The distribution of raindrops with size. *J. Meteor.* **5**, 165-166.
- Moorthi, S., and M. J. Suarez, 1992: Relaxed Arakawa-Schubert: A parameterization

- of moist convection for general circulation models. *Mon. Weather Rev.*, **120**, 978-1002.
- Raymond, D. J., S. K. Esbensen, C. Paulson, M. Gregg, C. S. Bretherton, W. A. Petersen, R. Cifelli, L. K. Shay, C. Ohlmann, P. Zuidema, 2004: EPIC2001 and the Coupled Ocean/Atmosphere System of the Tropical East Pacific, *Bull. Am. Met. Soc.*, **85**, 1341-1354.
- Reynolds, R. W., 1988: A real-time global sea surface temperature analysis. *J. Climate*, **1**, 75-86.
- Schubert S. D., M. J. Suarez, Y. H. Chang, and G. Branstator, The impact of ENSO on extratropical low-frequency noise in seasonal forecasts. *J. Climate*, **14**, 2351-2365, 2001.
- Schubert S. D., M. J. Suarez, P. J. Pegion, M. A. Kistler, and A. Kumar, Predictability of zonal means during boreal summer. *J. Climate*, **15**, 420-434, 2002.
- Simpson, J., 1971: On cumulus entrainment and one-dimensional models. *J. Atmos. Sci.*, **28**, 449-455.
- Slingo, J., 1987: The development and verification of a cloud prediction scheme for the ECMWF model. *Quart. J. Roy. Meteor. Soc.*, **113**, 899-927
- Simmons, A. J., and J. K. Gibson, 2000: The ERA-40 project plan *ERA-40 Project Series No. 1*, ECMWF Publications, Reading, U. K.
- Sparling, L. C., 2000: Statistical Perspectives on Stratospheric Transport. *Rev. Geophys.*, **38**, 417-436.
- Suarez, M. J. and L. L. Takacs, 1995: Documentation of the Aries/GEOS dynamical core Version 2. *NASA Technical Memorandum 104606*, **10**, 56pp.
- Sud, Y., and G. K. Walker, 1999: Microphysics of Clouds with the Relaxed Arakawa

- Schubert Scheme (McRAS). Part I: Design and Evaluation with GATE Phase III Data, 3196-3220.
- Sundqvist, H., 1988: Parameterization of condensation and associated clouds in models for weather prediction and general circulation simulation. *Physically Based Modelling and Simulation of Climate and Climatic Change*, M. E. Schlesinger, Ed., Reidel, 433-461.
- Tokioka, T., K. Yamazaki, A. Kitoh, and T. Ose, 1988: The equatorial 30-60 day oscillation and the Arakawa-Schubert penetrative cumulus parameterization. *J. Meteor. Soc. Japan*, **66**, 883-901.
- Wheeler, M., and G. N. Kiladis, 1999: Convectively coupled equatorial waves: Analysis of clouds and temperature in wavenumber-frequency domain. *J. Atmos. Sci.*, **56**, 374-399.
- Wu, X., X.-Z. Liang, and G. J. Zhang, 2003: Seasonal migration of ITCZ precipitation across the equator: Why can't GCMs simulate it? *Geophys. Res. Lett.*, **30**, 10.1029/2003GL017198.
- Xie, P., and P. Arkin, 1997: Global precipitation, a 17-year monthly analysis based on gauge observations, satellite estimates and numerical model outputs. *Bull. Am. Met. Soc.*, **78**, 2539-2558.
- Zhang, C. 2001: Double ITCZs. *J. Geophys. Res.*, **106**, 11,785-11,792.
- Zhang, G. J., and H. R. Cho, 1991: Parameterization of the vertical transport of momentum by cumulus clouds. Part I: Theory. *J. Atmos. Sci.*, **48**, 1483-1492.
- Zhang, M. H. and co-authors, 2004: Comparing clouds and their seasonal variations in 10 atmospheric general circulation models with satellite measurements (in preparation).

Zhou, J., Y. C. Sud and K.-M. Lau, 1996: Impact of orographically induced gravity-wave drag in the GLA GCM. *Quart. J. Roy. Meteor. Soc.*, **122**, 903-927.

Received _____

Exp.	Designation	Re-evaporation setting	Remarks	r	var
	B1	weak		0.70	1.52
	B2	moderate		0.81	1.21
	B3	strong		0.80	1.33
	H1	strong	Redistributed evap. cooling		
	M1	weak	Diffusive CMT		
	M2	moderate	Diffusive CMT		

Table 1: Summary of experiments performed. First column gives short hand designation. Second column gives indicates strength of re-evaporation. Third column indicates additional modifications to physical parameterizations. Fourth column gives pattern correlation of simulated precipitation with the CMAP climatology for a 7-season JJA 1981-87 mean. Fifth column is the rms error with respect to CMAP (mm d^{-1}) for the same period.

Exp.	Domain	\mathcal{P}_0 mm d ⁻¹	$\int \mathcal{R}$ (mm d ⁻¹)	$\mathcal{P}_0 + \int \mathcal{R}$	$\int \mathcal{R} / \mathcal{P}_0$		E_0	$E_0 - \mathcal{P}_0$
B1	SITCZ	6.157	3.220	9.376	0.5230	0.3434	5.429	-0.728
”	NITCZ	5.445	2.614	8.059	0.4801	0.3244	4.496	-0.949
”	WAFR	5.122	4.301	9.423	0.8399	0.4565	3.235	-1.887
”	SWUS	0.712	1.451	2.163	2.0367	0.6707	1.155	0.443
B2	SITCZ	4.804	6.801	11.605	1.4156	0.5860	5.402	0.598
”	NITCZ	5.066	5.863	10.929	1.1574	0.5365	4.687	-0.379
”	WAFR	4.575	7.335	11.910	1.6035	0.6159	2.554	-2.021
”	SWUS	0.525	2.730	3.256	5.1954	0.8386	0.894	0.368
B3	SITCZ	3.989	8.233	12.222	2.0640	0.6736	5.282	1.293
”	NITCZ	4.808	8.224	13.031	1.7106	0.6311	4.938	0.130
”	WAFR	3.944	8.436	12.379	2.1388	0.6814	2.349	-1.595
”	SWUS	0.479	2.761	3.240	5.7653	0.8522	0.762	0.283
H1	SITCZ	6.678	12.955	19.632	1.9400	0.6599	5.374	-1.304
”	NITCZ	4.574	8.943	13.517	1.9554	0.6616	4.972	0.399
”	WAFR	5.005	16.965	21.970	3.3899	0.7722	2.734	-2.270
”	SWUS	0.672	5.075	5.747	7.5466	0.8830	1.059	0.387
CMAP	SITCZ	4.636						
”	NITCZ	4.730						
”	WAFR	3.756						
”	SWUS	1.237						

Table 2: Domain averaged precipitation, re-evaporation and related quantities in 4 boxes illustrated in Figure 4 for JJA 1984-85. First column gives experiment designation from Table 1. Second column indicates Box for averages. Third column gives average precipitation \mathcal{P}_0 in mm d⁻¹. The fourth column gives the mass weighted vertical integral of moistening due to re-evaporation of falling precipitation, denoted by $\int \mathcal{R}$. This quantity is units of mm d⁻¹ and represents the additional rain that would reach the surface if not removed by re-evaporation. The fifth column is the sum $\mathcal{P}_0 + \int \mathcal{R}$, that is, the total precipitating condensate generated by autoconversion within a column. Columns 6 and 7 are ratios of $\int \mathcal{R}$ to \mathcal{P}_0 and $\int \mathcal{R} + \mathcal{P}_0$ respectively. Column 8 gives the average surface evaporation E_0 in units of mm d⁻¹. The 9-th column is the difference $E_0 - \mathcal{P}_0$. Positive numbers in this column indicate that the Box in question exports water horizontally to the rest of the atmosphere, while negative numbers mean water vapor must be imported to supply an excess of precipitation. The last 4 rows, labeled “CMAP”, give the observed precipitation in each box.

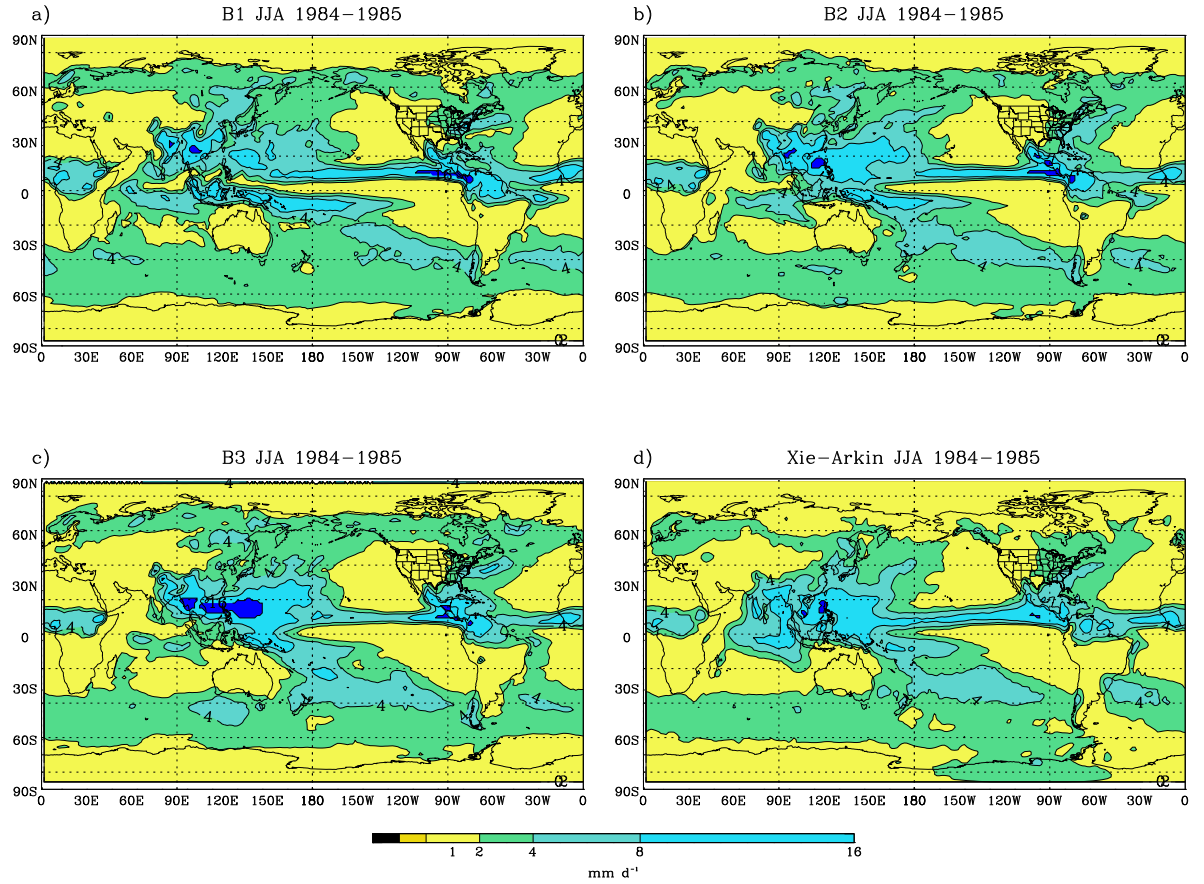


Figure 1: June-August (JJA) averages of precipitation for 1984-85: a) from Experiment B1 with weak re-evaporation, contours are drawn for 1.0, 2.0, 4.0, 8.0, and 16.0 mm d^{-1} ; b) as (a) except for Experiment B2 (moderate re-evaporation); c) as (a) except for Experiment B3 (strong re-evaporation); d) as (a) except for Xie-Arkin precipitation data.

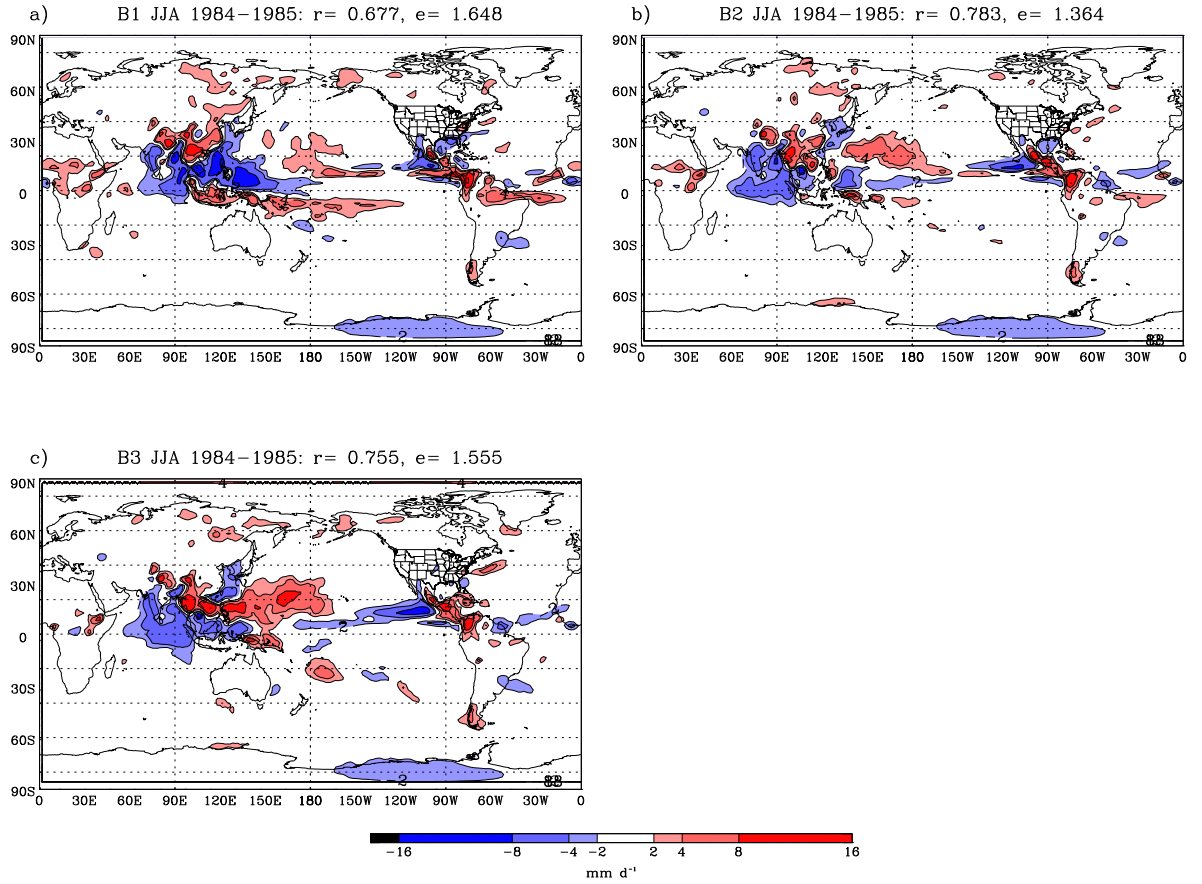


Figure 2: June-August (JJA) average precipitation biases with respect to Xie-Arkin (CMAP) climatology for 1984-85: a) Experiment B1 with weak re-evaporation, contours are drawn for -16, -8, -4, -2, 2, 4, 8, and 16 mm d^{-1} ; b) as (a) except for Experiment B2 (moderate re-evaporation); c) as (a) except for Experiment B3 (strong re-evaporation).

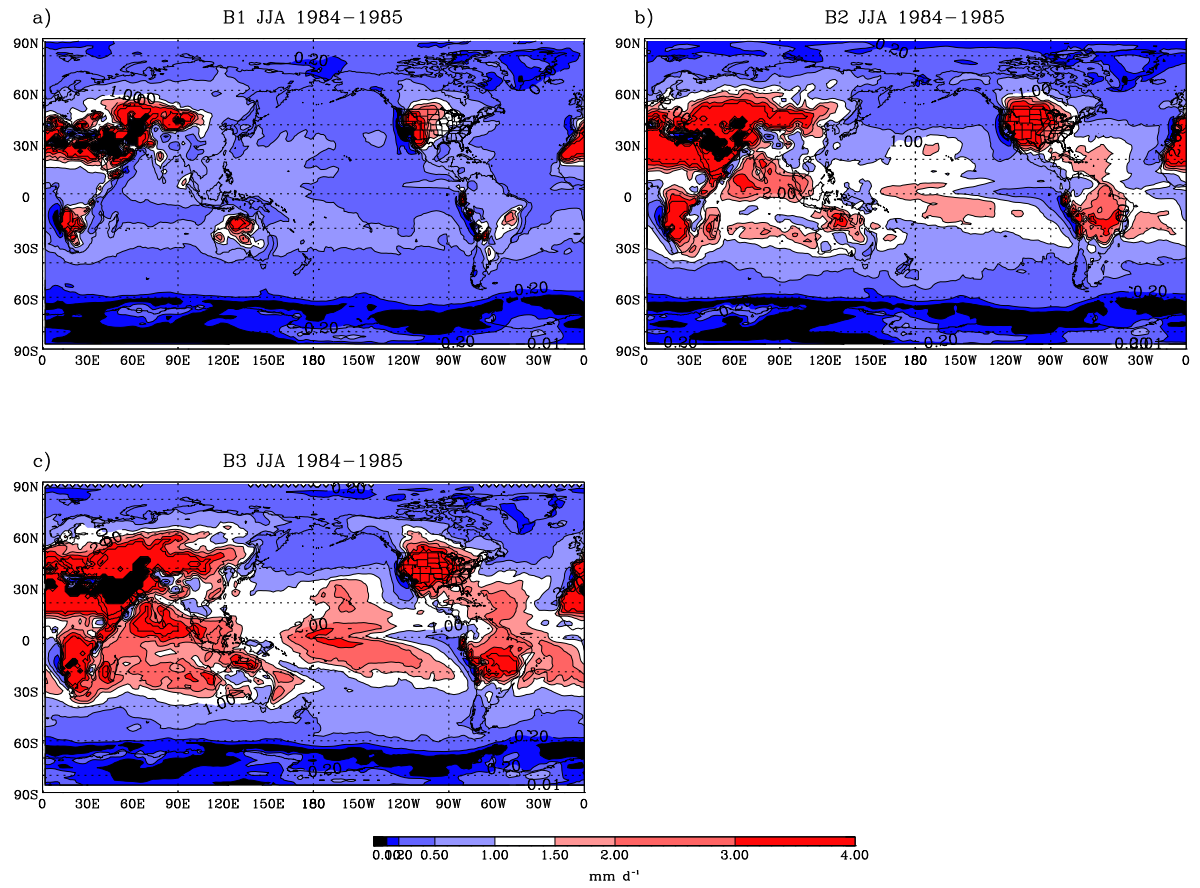


Figure 3: Ratio of re-evaporated precipitation to precipitation reaching the surface, f defined in (1). Seasonal means for JJA 1984-85 are shown: a) B1, weak re-evaporation; b) B2, moderate re-evaporation; and c) B3 strong re-evaporation.

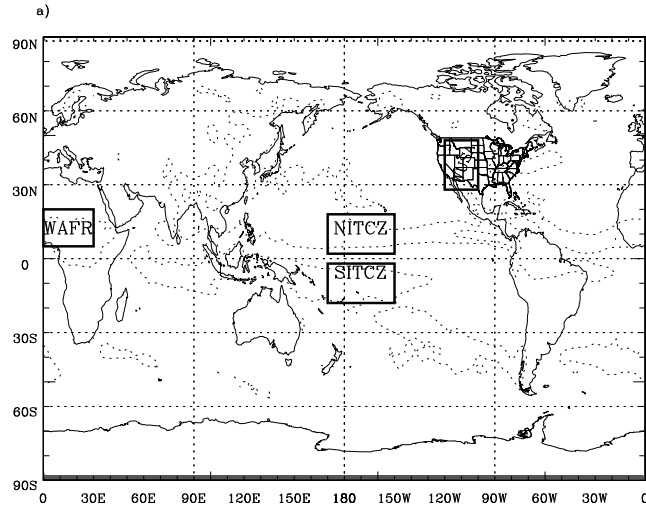


Figure 4: Boxes used for regional precipitation and evaporation calculations presented in Table 2. Four regions are defined; northern and southern Pacific ITCZ (NITCZ and SITCZ), tropical West Africa (WAFR), and the south-western US (WUSA).

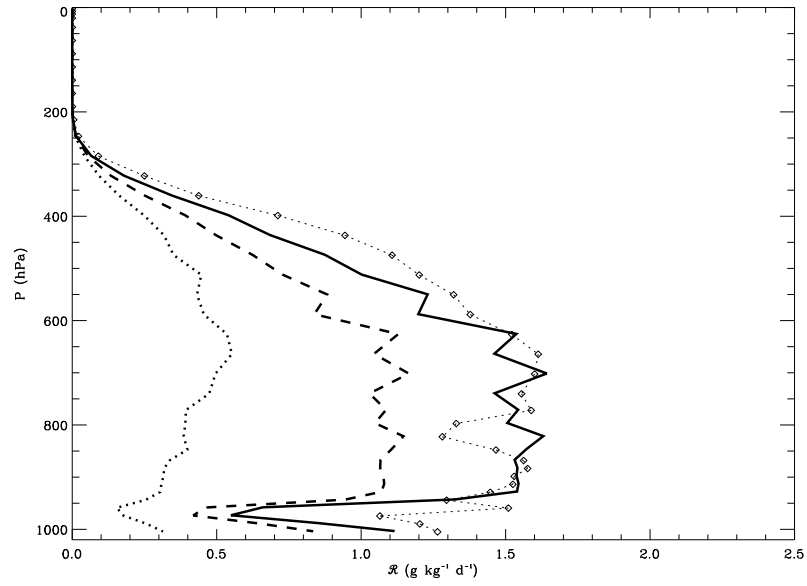


Figure 5: Mean profile of re-evaporation moistening \mathcal{R} in $\text{g kg}^{-1} \text{d}^{-1}$ for JJA 1984-85 in Box NITCZ. Solid line shows result for Exp B3 (strong \mathcal{R}), dashed line for B2 (moderate \mathcal{R}), dotted line for B1 (weak \mathcal{R}), and open diamonds for H1 (strong \mathcal{R} with modified cooling profile).

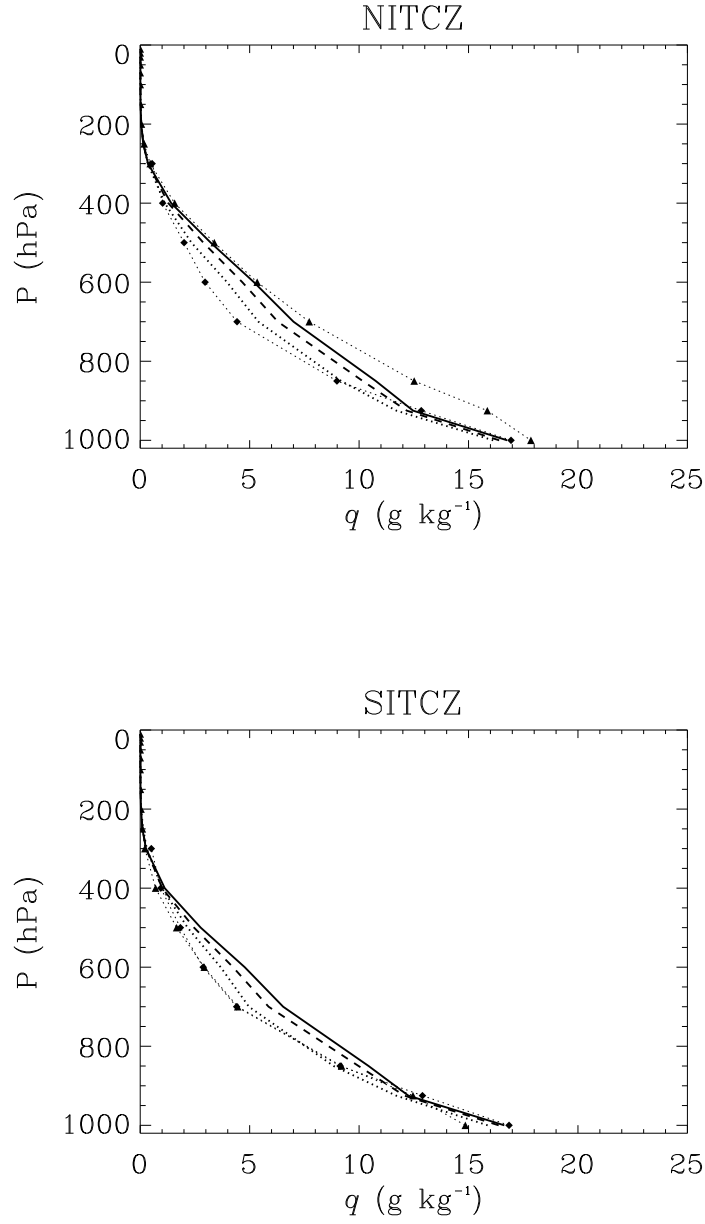


Figure 6: Specific humidity q in g kg^{-1} as a function of pressure in Boxes NITCZ (top) and SITCZ (bottom). Profiles are averages for JJA 1984/85. Solid lines show result for Exp B3, dashed lines for B2 and dotted lines for B1. Filled triangles show the ERA40 re-analysis q -profiles, and filled diamonds show q for the NCEP re-analysis.

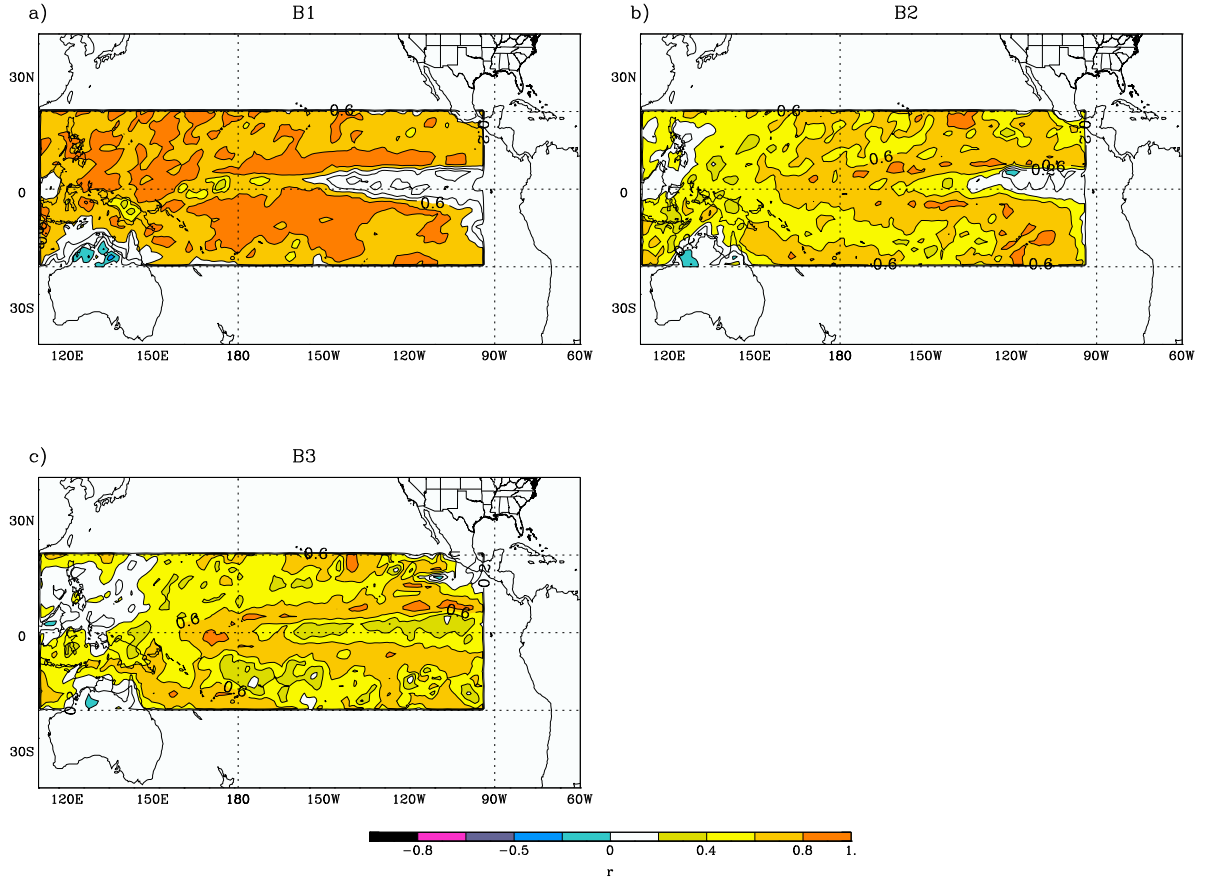


Figure 7: Correlation of daily 15-day, high-pass filtered vertical motion $\tilde{\omega}$ and precipitation $\tilde{\mathcal{P}}$ for April 1-Sept. 30 1984 and 1985: (a) for Exp B1 (weak re-evap.); (b) Exp B2; and (c) Exp B3

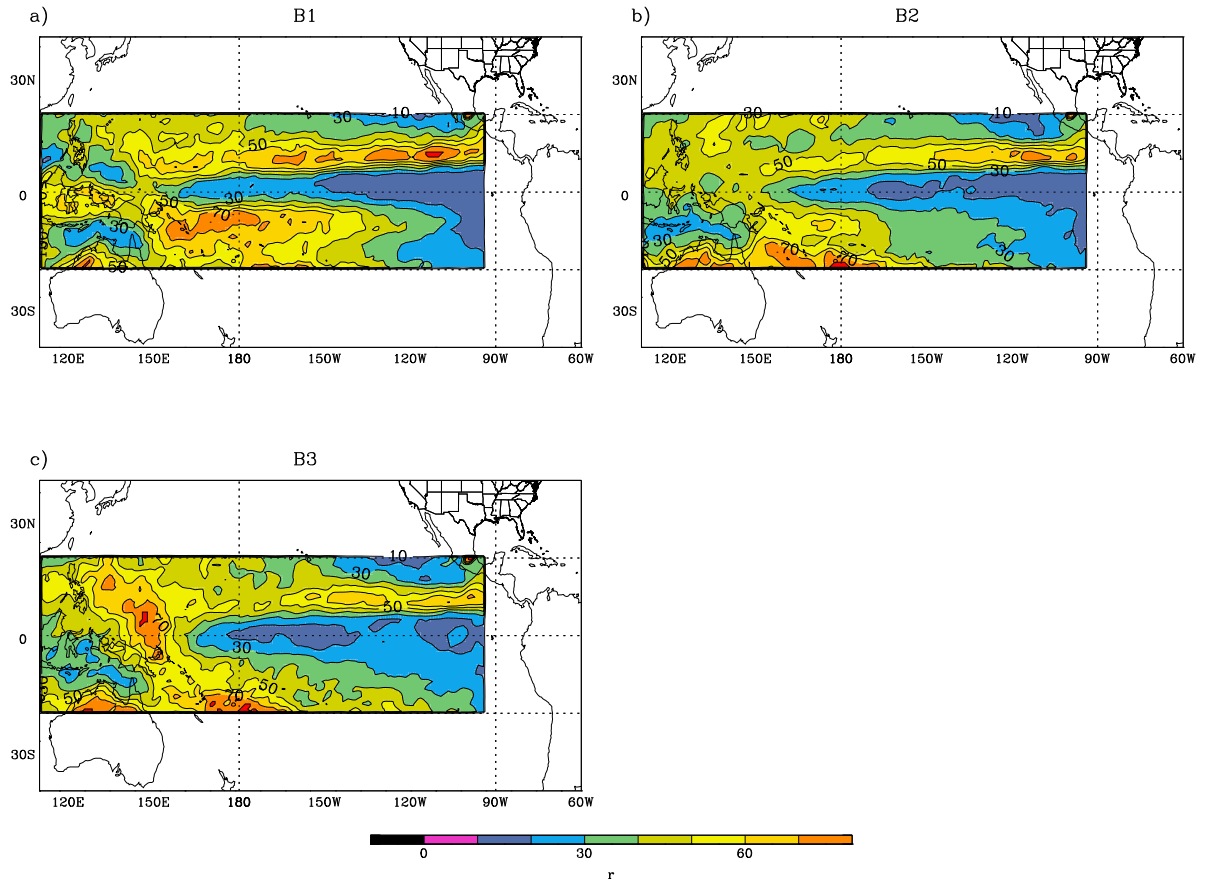


Figure 8: RMS value of 15-day high-pass filtered vertical motion field $\sqrt{\tilde{\omega}_{850}^2 t}$ for April 1-Sept. 30 1984 and 1985: (a) for Exp B1 (weak re-evap.); (b) Exp B2; and (c) Exp B3. Units are hPa d⁻¹.

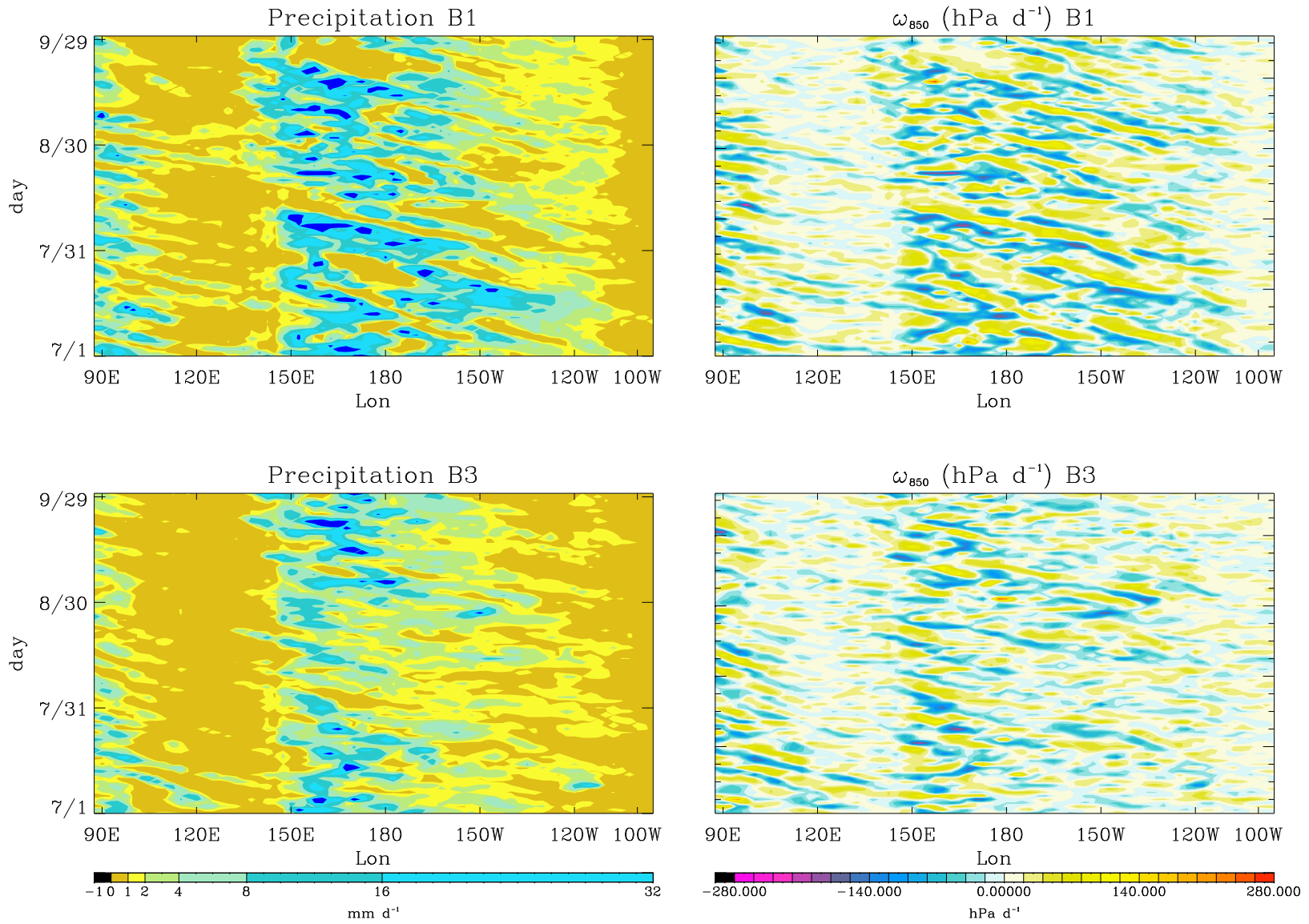


Figure 9: Hovmueller diagrams of vertical motion (right) and precipitation (left) along 10°S for JAS 1985 in Exp B1 (top) and B3 (bottom). 15-day, high-pass filtered vertical motion $\tilde{\omega}$ and unfiltered daily precipitation are shown.

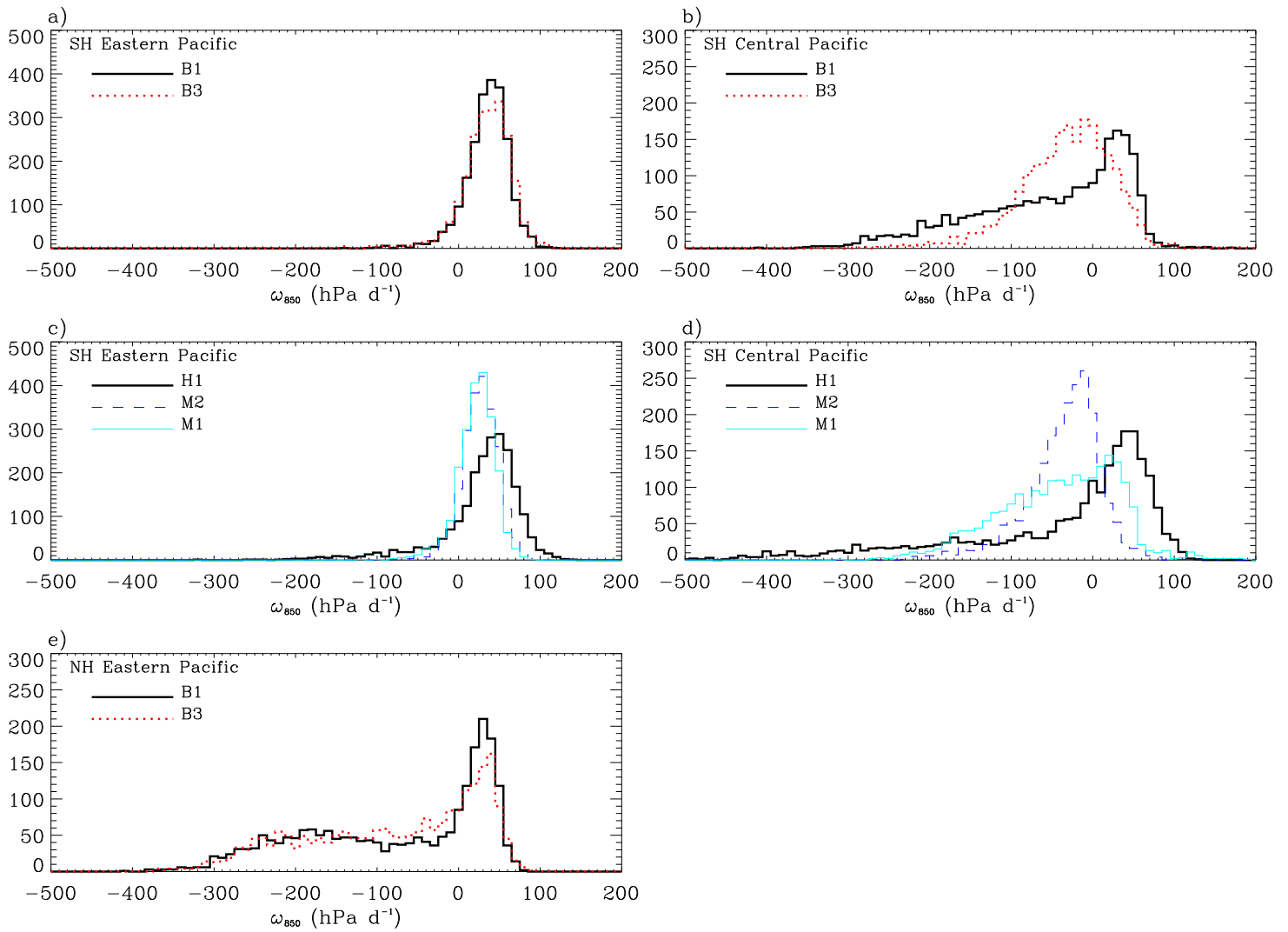


Figure 10: (a)-(d) Probability density functions (PDFs) of unfiltered, daily ω_{850} for JJA 1985 for two regions along the southern ITCZ. Top panels (a) and (b) show results for Exps B1 (solid black curve) and B3 (dashed red). Bottom panels (c,d) show results for perturbed physics experiments H1 (solid black), M1 (solid light blue) and M2 (dashed dark blue). Left panels (a) and (c) show PDFs for a region in the eastern Pacific, between 12°S and 6°S bounded by 110°W and 97.5°W . This region immediately off of the coast of S. America is meant to represent atmospheric variability that is as yet relatively unaffected by interactions between moist heating and dynamics. Sharp peaks at small positive values indicate ubiquitous weak subsidence. Right panels (b) and (d) show PDFs for a region in the central Pacific, between 12°S and 6°S bounded by 162.5°E and 175°E . Panel (e) shows PDFs for B1 and B3 for a box in the eastern portion of the northern ITCZ (6°N - 12°N , 110°W - 97.5°W), for comparison

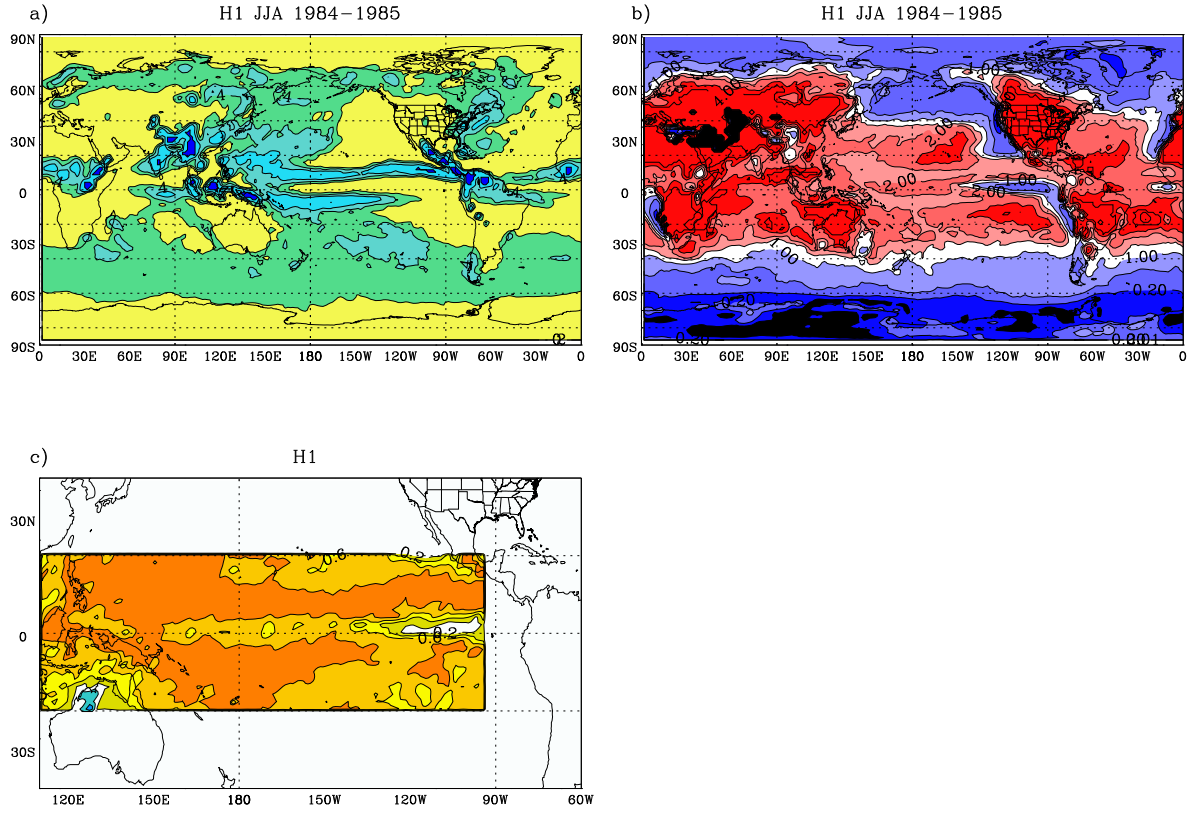


Figure 11: (a) Seasonal mean JJA 1984-85 precipitation for Exp H1, scale as in Fig.1; (b) f , fraction of re-evaporated rain to surface rain, scale as in Fig. 3; and (c) Correlation of $\tilde{\omega}$ and \tilde{P} time-series for April 1-Sept. 30 1984 and 1985, scale as in Fig. 7

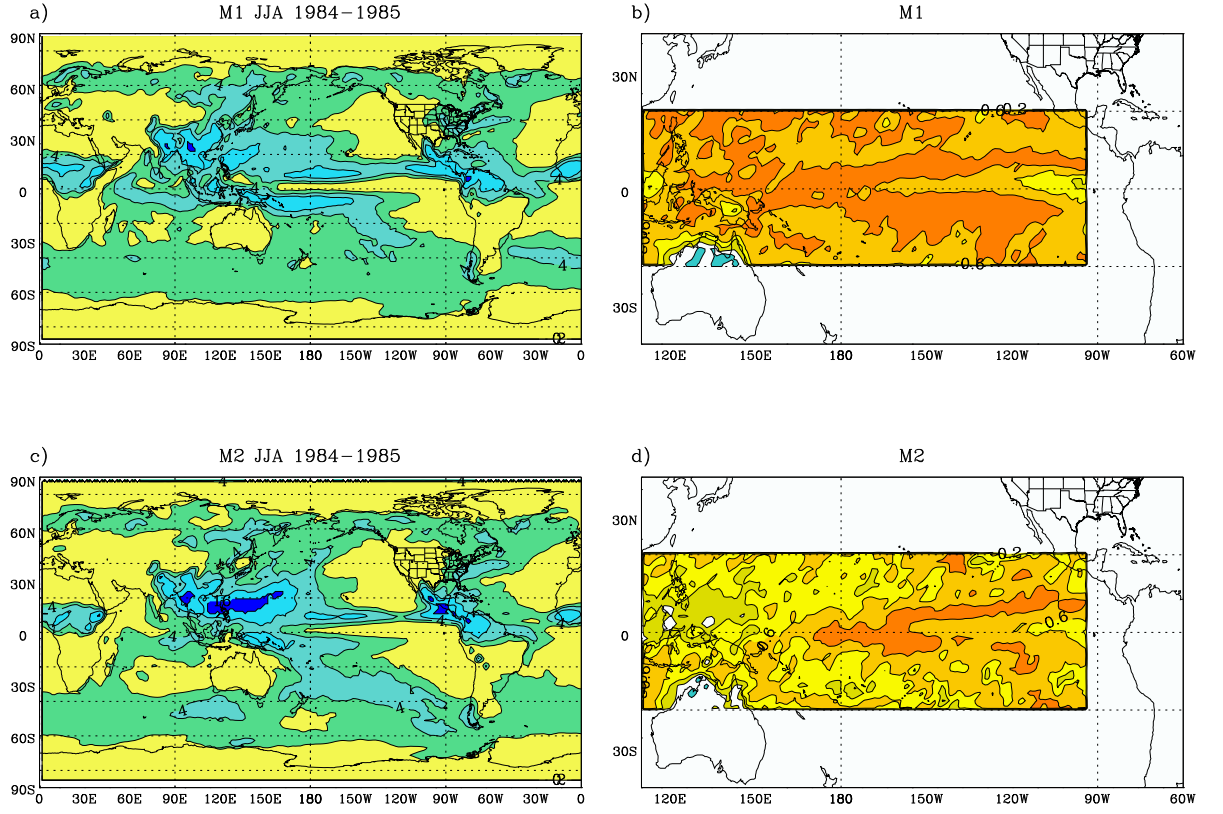


Figure 12: (a) JJA 1984-85 precipitation for Exp M1. (b) Correlation of daily $\tilde{\omega}$ and \bar{P} time-series for April 1-Sept. 30 1984 and 1985 in Exp M1 (c) as (a) for Exp M2. (d) as (b) for Exp M2. Scales for (a) and (c) are as in Fig. 1. Scales for (b) and (d) are as in Fig. 7.

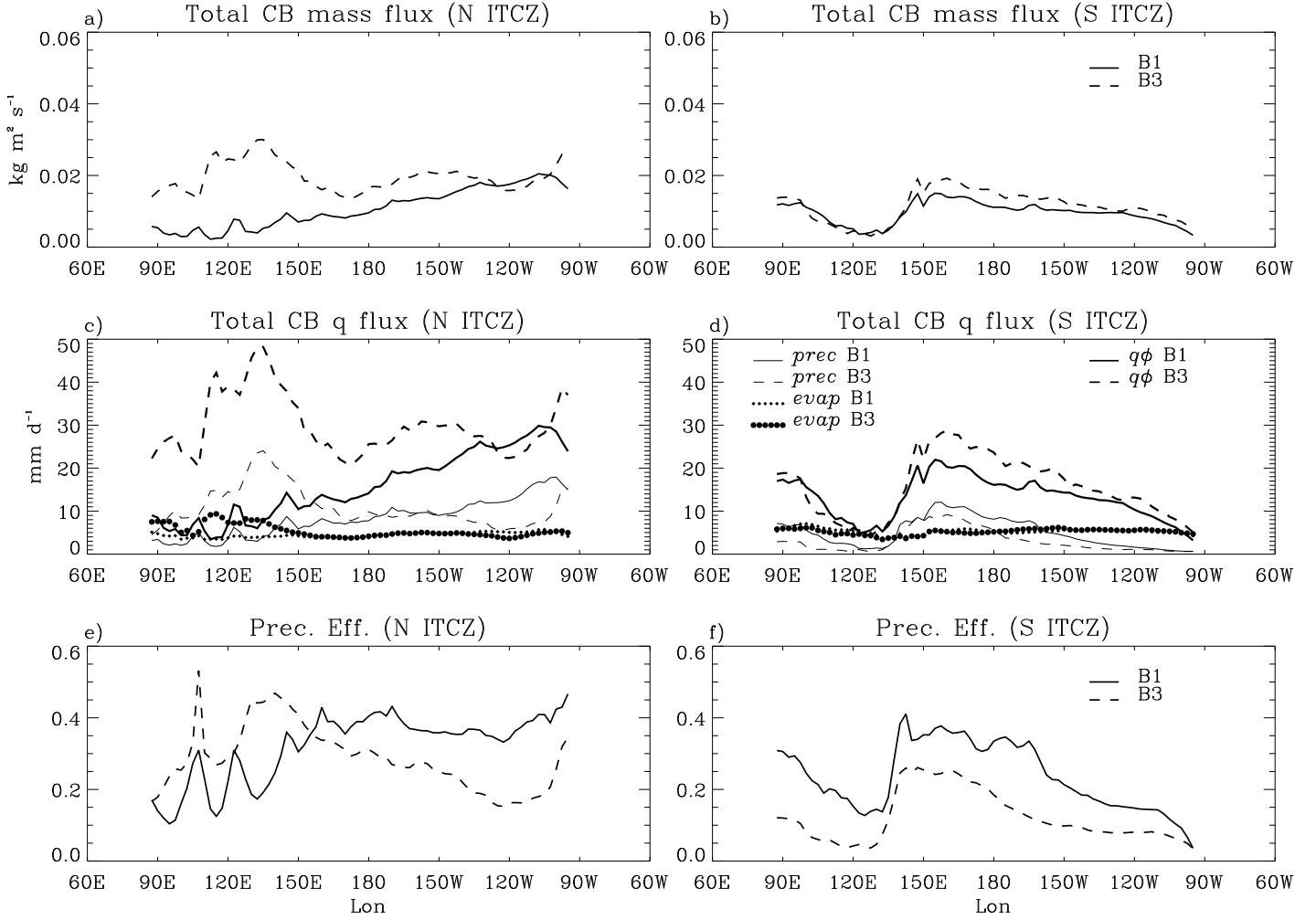


Figure 13: Convective Mass and moisture fluxes, and precipitation efficiency for JJA 1985 in B1 B3, along northern 8-14 °N (left panels) and southern 12-6 °S (right panels) ITCZs. Key for lines in each row is shown in right panels. Panels (a) and (b) show cloud base mass flux, summed over all cloud types invoked by RAS. Panels (c) and (d) show diagnosed cloud base convective moisture fluxes (thick solid and dashed lines). Thin solid and dashed lines in (c) and (d) show precipitation. Symbols in (c) and (d) show surface evaporation - large circles correspond to Exp B3, small diamonds to B1. Panels (e) and (f) show the ratio of precipitation to convective moisture flux at cloud base.

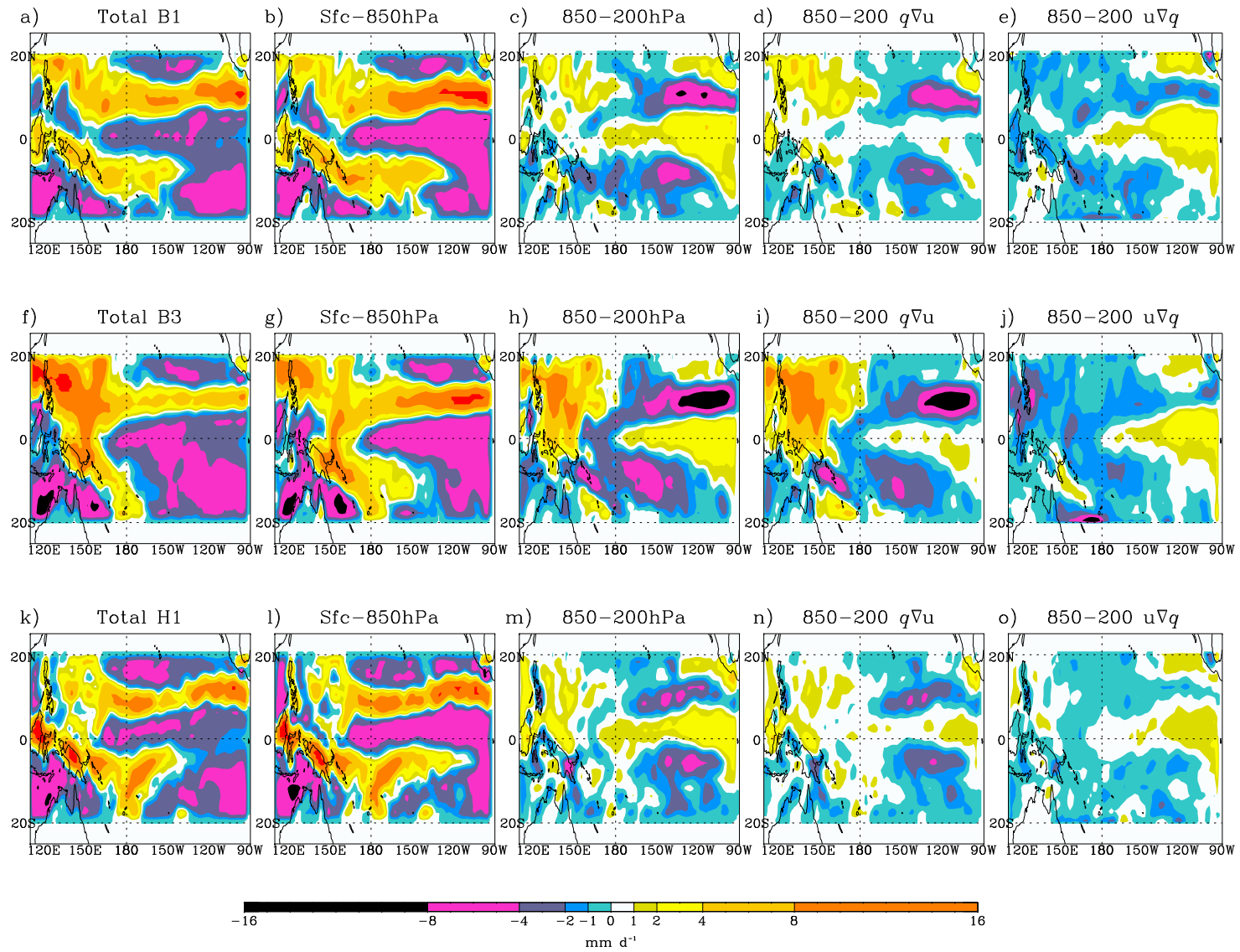


Figure 14: Mean, vertically-integrated, horizontal transport tendencies for water vapor defined in (2)-(4) of the text, as functions of longitude and latitude. Results are shown for JJA 1985; in Exp B1 top row, (a)-(e); B3, middle row, (f)-(j); and H1, bottom row, (k)-(o). All quantities are displayed in units of mm d^{-1} . The first column, (a), (f), and (k), shows total, column-integrated water vapor flux convergence \mathcal{T}_1^0 ; (b), (g), and (l), $\mathcal{T}_1^{0.85}$, water vapor flux convergence in the layer bounded by $\sigma=1$ and $\sigma=0.85$; (c), (h), and (m), $\mathcal{T}_{0.85}^{0.2}$, water vapor flux convergence in the layer bounded by $\sigma=0.85$ and $\sigma=0.2$; (d), (i), and (n), $\mathcal{C}_{0.85}^{0.2}$, water vapor transport by large-scale convergent flow between $\sigma=0.85$ and $\sigma=0.2$; (e), (j), and (o), $\mathcal{A}_{0.85}^{0.2}$, advective water vapor transport between $\sigma=0.85$ and $\sigma=0.2$.

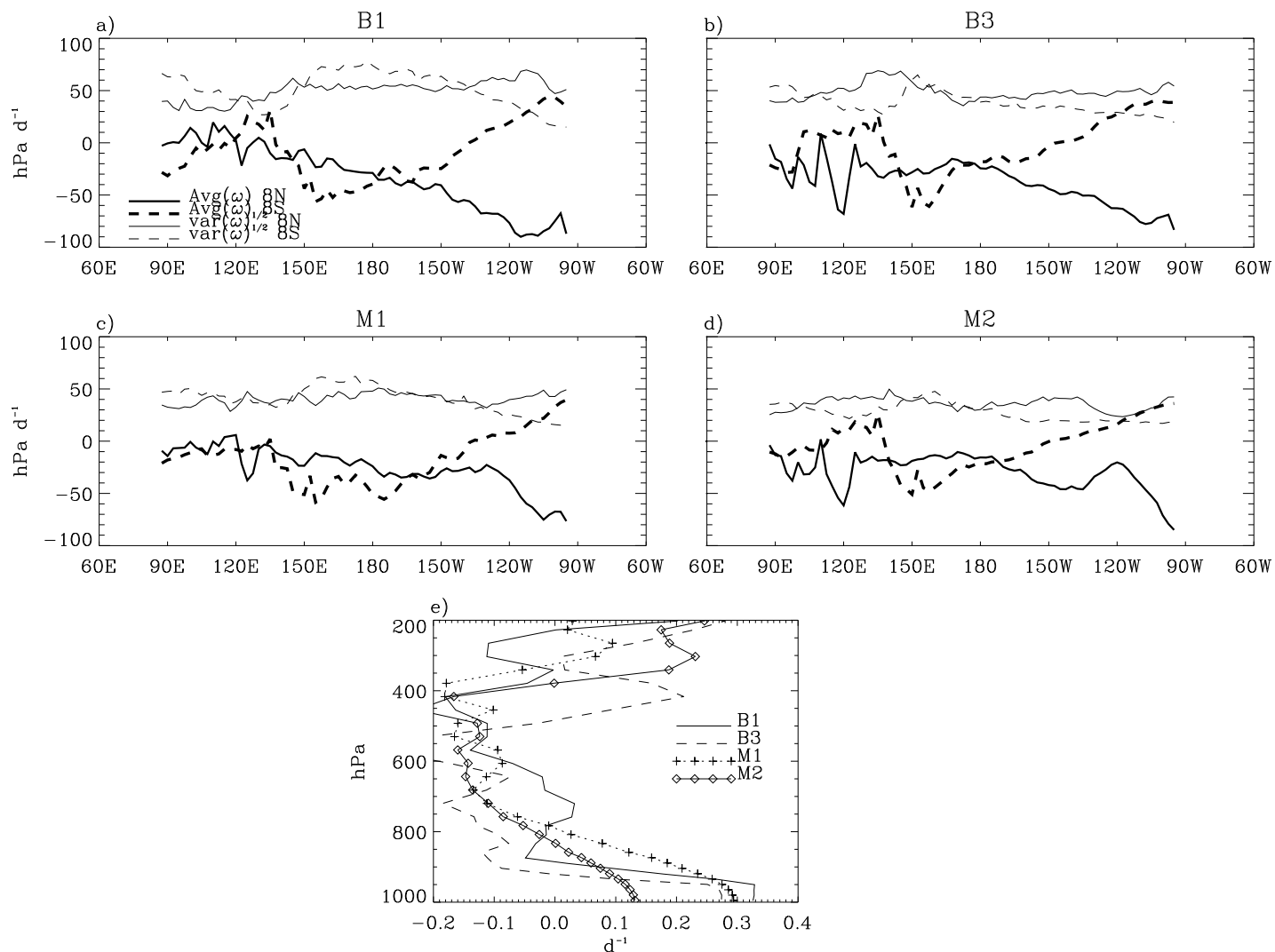


Figure 15: (a-d) Mean Vertical motion $\overline{\omega_{850}}$ and rms amplitude of 15-day high-pass, filtered vertical motion $\sqrt{\overline{\omega_{850}^2}}$, as functions of longitude along 8°N and 8°S, for JJA 1985 in (a) Exp B1, (b) B3, (c) M1 and (d) M2. Line key for panels (a)-(d) is shown in (a). Panel (e) shows vertical profiles of time mean convergence $\partial_p \omega$ (d^{-1}) at a location in the core of the southern ITCZ.